

Article

Acoustic Dispersion in Low Permeability Unconventional Reservoir Rocks and Shales at In Situ Stress Conditions

Sheyore John Omovie ^{1,*}, Mike Myers ² and John P. Castagna ³¹ Formerly with Oxy, 5 Greenway Plaza, Houston, TX 77046, USA² Department of Petroleum Engineering, Cullen College of Engineering, University of Houston, 5000 Gulf Freeway, Houston, TX 77204, USA³ Department of Earth and Atmospheric Sciences, College of Natural Sciences and Mathematics, University of Houston, 3507 Cullen Blvd, Houston, TX 77204, USA

* Correspondence: john.omovie@physics.org

Abstract: Utilizing laboratory measurements on dry and fully brine-saturated well-lithified shale reservoir rocks and comparing them to log data and theoretical modeling, we find no statistically significant intrinsic dispersion from seismic to sonic and laboratory measurement frequencies due to fluid effects. Under in situ stress conditions, the Gassmann zero-frequency P-wave velocity prediction for a Permian basin sample was within 0.3% of the measured velocity on the brine-saturated sample at an ultrasonic frequency. At deviatoric stresses ranging from 1.7 to 70 MPa on the same sample, the percent error in the Gassmann P-wave velocity prediction ranges from 0.3 to 2.2%. These results are consistent with the lack of significant dispersion in the reported velocities and theoretical predictions in the Cotton Valley shale. Based on the Biot–Gassmann model, the characteristic frequency in both formations occurs at $\sim 10^{10}$ Hz. Applying a squirt flow model also predicts transition to the high-frequency regime occurring at $\sim 10^9$ Hz for both formations. The comparison of the sonic log measurements for four different shale/tight rock formations to ultrasonic measurements taken from core samples under in situ stress conditions confirms these findings. To our knowledge, this is the first extensive comparison of the sonic log to ultrasonic core data measurements. For these rocks, there is no clearly observable or predicted significant dispersion due to fluid effects at in situ stress conditions within the frequency range for which measurements are made.

Keywords: shale reservoir; acoustic-wave dispersion; Biot–Gassmann; squirt-flow; ultrasonic frequency



Citation: Omovie, S.J.; Myers, M.; Castagna, J.P. Acoustic Dispersion in Low Permeability Unconventional Reservoir Rocks and Shales at In Situ Stress Conditions. *Minerals* **2022**, *12*, 1180. <https://doi.org/10.3390/min12101180>

Academic Editors: Stanislaw Mazur, Xianguo Zhang, Hongliu Zeng, Muhammad Jawad Munawar, Tao Zhang and Youjing Wang

Received: 23 May 2022

Accepted: 13 September 2022

Published: 20 September 2022

Publisher's Note: MDPI stays neutral with regard to jurisdictional claims in published maps and institutional affiliations.



Copyright: © 2022 by the authors. Licensee MDPI, Basel, Switzerland. This article is an open access article distributed under the terms and conditions of the Creative Commons Attribution (CC BY) license (<https://creativecommons.org/licenses/by/4.0/>).

1. Introduction

Acoustic-wave dispersion is observed in fluid-saturated porous and permeable sedimentary rocks (e.g., [1–4]). Wang and Nur (1990) [1], for example, reported dispersion in rocks saturated with low viscosity fluids as high as 5%. Sams et al. (1997) [5] observed a similar effect when measurements were made at seismic, sonic, or ultrasonic frequencies. A similar dispersion magnitude has been reported for laboratory measurements made over a wide range of frequencies (Spencer, 1981) [3]. The question then arises as to the significance of dispersion in low-permeability unconventional reservoir rocks and shale formations. With the increased interest in the development of unconventional reservoir rocks, it is necessary to address whether dispersion correction is necessary when comparing acoustic measurements made at different frequencies. For example, could ultrasonic laboratory measurements made on core samples be directly compared to sonic log measurements without first applying dispersion correction? For the Bakken shale formation, based on theoretical predictions using Biot (1956) [6] and squirt-flow models [2], Liu et al. (1994) [7] concluded that seismic, sonic, and ultrasonic frequencies are in the same frequency regime; if true, intrinsic dispersion correction is unnecessary. Sarker and Batzle (2010) [8] and Hofmann (2005) [4], based on experimental observations in the 2 Hz to 0.8 MHz frequency range, also did not observe significant dispersion in Mancos Shale and a West African shale,

both having low porosity. On the other hand, Szewczyk et al. (2017) [9] observed significant dispersion based on laboratory measurements on Mancos and Pierre shale core samples from outcrop. Hofmann (2005) [4] also observed significant dispersion on a West Africa shale sample with high porosity.

In addition, in the development of unconventional reservoirs, static elastic properties are often required to create geomechanical models to aid with drilling through shale formations to avoid wellbore stability issues [10]. These static elastic properties are also needed in hydraulic fracture designs to optimize the exploitation of the reservoir. Ideally, the static elastic properties are determined from the static triaxial measurements made on the core samples. However, these measurements are limited due to core availability and cost constraints. Instead, dynamic moduli (computed from sonic log measurements and ultrasonic laboratory measurements) are usually used to estimate static moduli after calibration to measured static moduli [11,12]. It is thus necessary to address the question: What impact if any, does dispersion have on the dynamic versus static elastic moduli relationship used in geomechanical models?

We performed calculations based on Biot flow and squirt flow and then compared them to the measurements made both in the laboratory at ultrasonic frequencies (~1 MHz) and in the field at sonic frequencies (10–30 KHz). Our focus was to determine if dispersion effects occur under in situ stress conditions. Our method is similar to the approach adopted by Wang and Nur (1990) [1] and Winkler (1985) [13]. This approach allowed us to quantify the presence of dispersion. The initial assumption is that there is virtually no velocity dispersion in dry rocks, consistent with Spencer (1981) [3] and Peselnick and Outerbridge (1961) [14]. Using this method, we attempted to answer the following three questions:

1. Does the low-frequency Gassmann equation adequately predict the change that will result if a rock sample containing gas were fully saturated with brine?
2. Do we observe dispersion in these rocks when we compare ultrasonic measurements made in the laboratory to sonic log measurements made in the field?
3. Does the Biot–Gassmann or the squirt-flow model accurately predict the presence or absence of dispersion in these low-permeability formations at the frequency range used in the petroleum industry? Here we define low permeability as a rock with a permeability of the order of 1 microdarcy or lower.

We address these questions for four different unconventional reservoir rock/shale formations, including Bonespring sand, two Wolfcamp shale formations, and the Lower Spraberry shale. The Bonespring sand is a tight shaly sand formation in the Delaware basin—a sub-basin of the Permian basin—often described as a hybrid shale–oil system. Lower Spraberry shale is a Permian age organic-rich volatile oil shale from the Midland basin—a sub-basin of the Permian basin. Wolfcamp shale is also a Permian-age organic shale from the Midland basin. Lastly, there is the other Permian age Wolfcamp shale from the Delaware basin.

2. Materials and Methods

2.1. Biot–Gassmann Model

The Biot–Gassmann model does not predict dispersion in dry rock samples. As discussed, this is evident from work undertaken by Spencer (1981) [3]. Spencer measured acoustic-wave velocities in the laboratory from 4 to 400 Hz on sandstone, limestone, and granite rock samples. He found that there is negligible dispersion in the dry samples independent of lithology, while the fluid-saturated samples showed significant dispersion. Peselnick and Outerbridge (1961) [14] also observed negligible dispersion in dry rocks over a much wider frequency range. Winkler (1985) [13] compared laboratory-measured dry and saturated velocities to investigate the dispersion in Berea sandstone and observed significant dispersion. These investigations, which show dispersion, are all in more porous and permeable samples than investigated here.

Given the acoustic measurements made on a dry sample, we determined the frame bulk and shear moduli. The mineral matrix modulus was determined using the Voigt–Reuss–Hill

average of the constituents' lithologies matrix modulus. The Hill average is known to yield fairly accurate effective elastic moduli when the bounds are narrow, which occurs when the elastic properties of the constituent minerals do not differ significantly [15,16]. The Hill average is:

$$K_m = 0.5 \left(\left\{ \sum_{i=0}^L X_i K_i \right\} + \left\{ \sum_{i=0}^L X_i / K_i \right\}^{-1} \right) \quad (1)$$

where K_m is the matrix bulk modulus, L is the number of pure mineral components making up the solid fraction, X_i is the fraction of solid volume occupied by mineral component i , and K_i is the bulk modulus of the pure mineral component i .

The Gassmann fluid-saturated zero-frequency equation is:

$$K_c = K_{fr} + \frac{\left(1 - \frac{K_{fr}}{K_m}\right)^2}{\Omega - \frac{K_{fr}}{K_m^2}} \quad (2)$$

where $\Omega = \frac{\varnothing_t}{K_f} + \frac{(1-\varnothing_t)}{K_m}$ and where K_{fr} is the frame bulk modulus, \varnothing_t is the total porosity, and K_f is the fluid bulk modulus. From Equation (2), the fluid-saturated low-frequency P-wave velocity can be determined given the rock bulk density and shear modulus.

For the Biot high-frequency limit prediction, we used the Geerstma and Smit (1961) [17] approximation, for which the Biot high-frequency limit P-wave velocity ($V_{p\infty}$) is given by:

$$V_{p\infty} = \left\{ \frac{1}{\rho_m(1-\varnothing_t) + \varnothing_t \rho_{fl}(1-\alpha^{-1})} \left[\left(K_{fr} + \frac{4}{3} G_{fr} \right) + \frac{\varnothing_t \frac{\rho}{\rho_{fl}} \alpha^{-1} + \left(1 - \frac{K_{fr}}{K_m}\right) \left(1 - \frac{K_{fr}}{K_m} - 2\varnothing_t \alpha^{-1}\right)}{\left(1 - \frac{K_{fr}}{K_m} - \varnothing_t\right) \frac{1}{K_m} + \frac{\varnothing_t}{K_{fl}}} \right] \right\}^{1/2} \quad (3)$$

where ρ_m is the grain density, ρ_{fl} is the fluid density, G_{fr} is the frame shear modulus, and α is the tortuosity parameter.

The Biot characteristic frequency is given by:

$$f_c = \frac{\mu \varnothing_t}{2\pi k \rho_{fl}} \quad (4)$$

where μ is the viscosity and k is the permeability. Since the permeability is in the denominator, all else being constant, the lower the permeability, the higher the characteristic frequency. This is important for our very low-permeability samples.

Following the approach adopted by Winkler (1985) [13] and Wang and Nur (1990) [1], we defined the Biot dispersion as the percent difference between the Gassmann zero-frequency velocity prediction and the Biot high-frequency velocity prediction. The apparent dispersion is defined as the percent difference between the measured velocity at ultrasonic frequency and the Gassmann prediction. Thus,

$$D_A = \left[\frac{V_M - V_G}{V_G} \right] * 100 \quad (5)$$

and

$$D_B = \left[\frac{V_B - V_G}{V_G} \right] * 100 \quad (6)$$

where D_A is the percent of apparent dispersion, V_M is the measured velocity, V_G is the Gassmann zero- frequency velocity prediction, V_B is the Biot high-frequency velocity prediction, and D_B is the percent Biot dispersion.

2.2. S squirt-Flow Model

The squirt-flow mechanism is based on experimental observations that, which at high enough effective pressures, Biot's theory is sufficient to explain the small velocity dispersion

observed, while at lower effective stresses, the compliant pores are still open and are the source of the increased dispersion [2,18]. As the rock is deformed by the passage of an acoustic wave, some pores may close while others may open. This can produce localized variations in pore pressure, which will cause fluids to “squirt” out of the closing pores.

Building on earlier work undertaken by Mavko and Jizba (1991) [18], Shapiro (2003) [19], Gurevich et al. (2010) [20], and de Paula et al. (2012) [21] showed that the measured velocities in the dry rocks and the compressibility computed from them at varying stresses are related to the closure of the compliant and intermediate (moderately stiff) pores. They showed that the squirt flow between these intermediate pores and stiff pores is responsible for the dispersion observed under ultrasonic frequencies.

Our implementation of this model was based on the work of Dvorkin et al. (1995) [2]. Because of the squirt-flow model’s complexity, we refer the reader to Appendix E in Dvorkin et al. (1995) [2]. An explanation of the implementation is discussed in the method section. In the discussion section, we show that similar results would be expected if we had implemented the Gurevich et al. (2010) [20] and de Paula et al. (2012) [21] approach.

2.3. Sample Description

Our measurements were performed on a Permian-age unconventional reservoir rock from the Delaware basin, a sub-basin of the Permian basin. The whole core from which the sample was cut was acquired from a depth of about 3110 m. Sample damage was minimized by careful handling.

The sample composition, determined from X-ray diffraction (XRD), is shown in Table 1. The 23.2% volume fraction of the clay is composed primarily of illite (20%), and the remaining 3.2% is made up of kaolinite and chlorite. The sample’s dimensions were 1” in diameter and 2” in length.

Table 1. (a) Composition from XRD of the core sample. (b) Constituent mineral bulk modulus used in determining matrix modulus.

(a)	
Mineralogy	Volume (%)
Quartz	51.0
K-Feldspar	4.0
Plagioclase	13.3
Calcite	2.5
Fe-Dolomite	4.5
Pyrite	1.5
Illite and Mica	20.0
Kaolinite	0.5
Chlorite	2.7
(b)	
Mineralogy	Bulk Modulus (GPa)
Quartz + Feldspars	38.00
Calcite	64.51
Dolomite	91.76
Clays (Illite)	52.60
Pyrite	147.63

The sample was vacuum dried at 80 degrees Celsius for several days until the sample weight stabilized. Figure 1 is a cross plot of sample weight versus time in hours while drying the sample. The measured permeability of a twin sample is 0.2 microDarcy, and the porosity is 5.65%, using the GRI method [22]. The in situ overburden stress was estimated from the density log to be 72.4 MPa. The estimated pore pressure was 34.47 MPa, and the estimated horizontal stress was 55.16 MPa, leading to an estimated mean effective horizontal stress of 20.68 MPa.

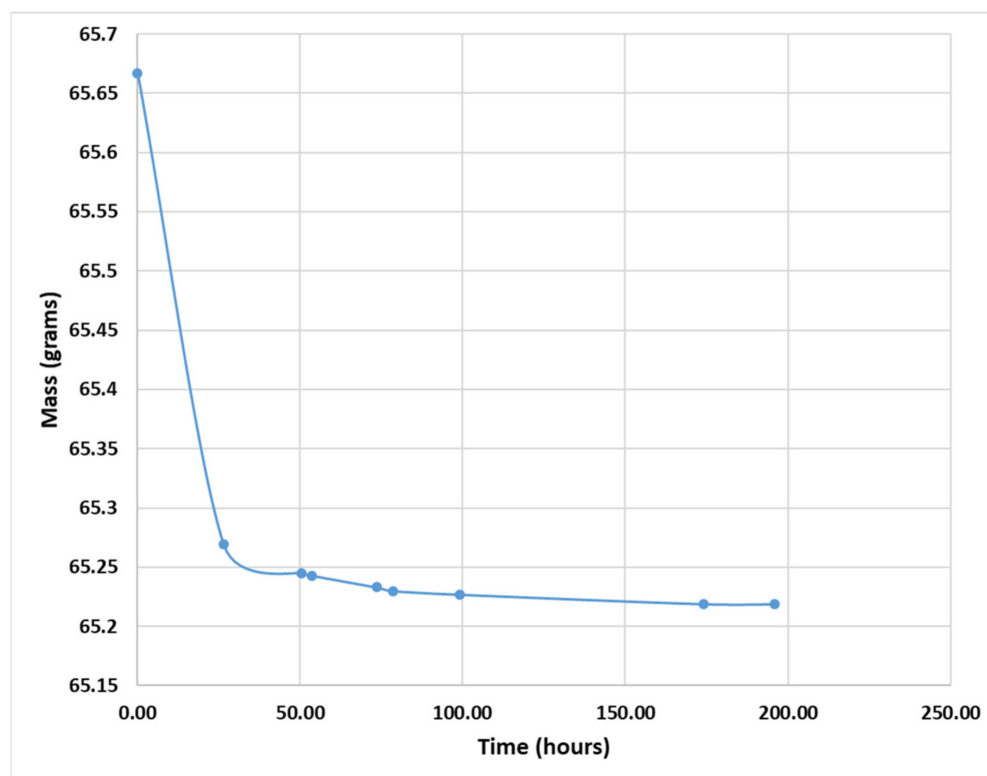


Figure 1. Sample weight versus time while drying the sample.

Table 1 shows the constituent mineral bulk modulus used in computing the matrix bulk modulus.

2.4. Experimental Procedure

To prevent the confining fluid from penetrating the dry sample, the sample was jacketed in an impermeable sleeve after being wrapped in a wire mesh. The sample was mounted between acoustic transducers, and the assembly was placed in a tri-axial cell, as shown in Figure 2a. Based on a prior tri-axial test on a twin sample, we determined the rock sample elastic limit to be ~110 MPa under a confining stress of 20.68 MPa. A drained tri-axial test was carried out on the dry sample under deviatoric stresses below the elastic limit of the rock. The irrecoverable strain was 0.12%, indicating minimal sample damage. Ultrasonic P-wave and S-wave velocity measurements were made during the tri-axial experiment. The confining stress was kept constant at 20.68 MPa, while the deviatoric stresses (difference between axial and confining stress) varied from zero to about 89.6 MPa, well below the maximum compressive strength of the twin sample, which was 193 MPa. The application of deviatoric stress is a better approximation to the sub-surface stress state than an isostatic stress test. We used the acoustic data acquired during the loading cycle for our analysis. As shown in Figure 3a,b, the bedding-normal P-wave and S-wave velocities were computed from the recorded P-wave and S-waveforms. The sample weight prior to the experiment on the dry sample was 65.22 g, and the post-test sample weight was 65.23 g.

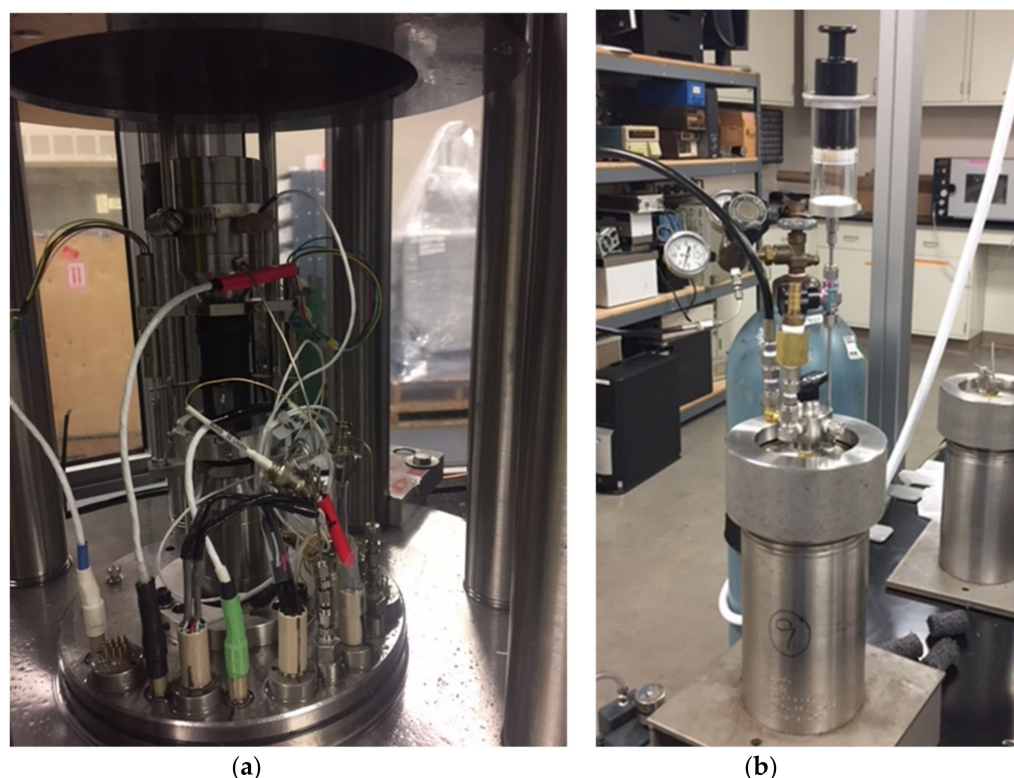
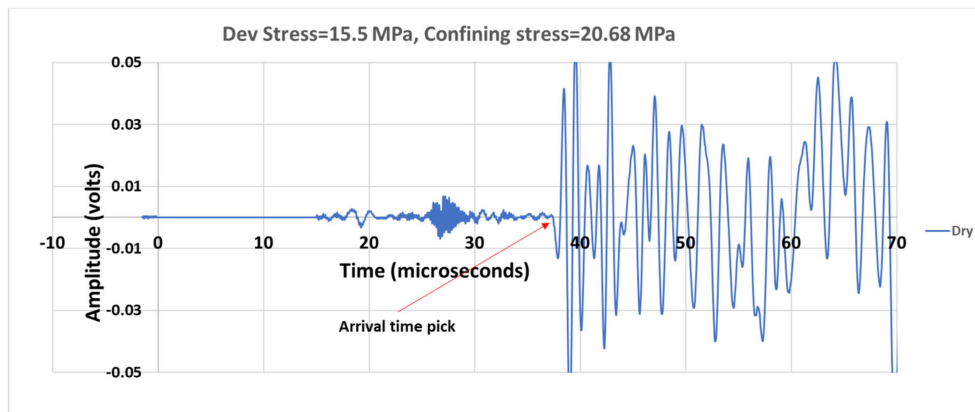


Figure 2. (a) Experimental setup for the dry and brine-saturated sample. Internal instrumentation includes load cell to measure deviatoric stress, 2 LVDTs (Linear variable differential transformer) for measurement of axial strain, a radial cantilever bridge, and end caps housing the P and S-wave 1 MHz piezoelectric transducer. (Equipment provided by MetaRock[®] laboratories). (b) Pressure vessel where sample was saturated; apparatus allows for first vacuum evacuating the sample before saturating with brine.

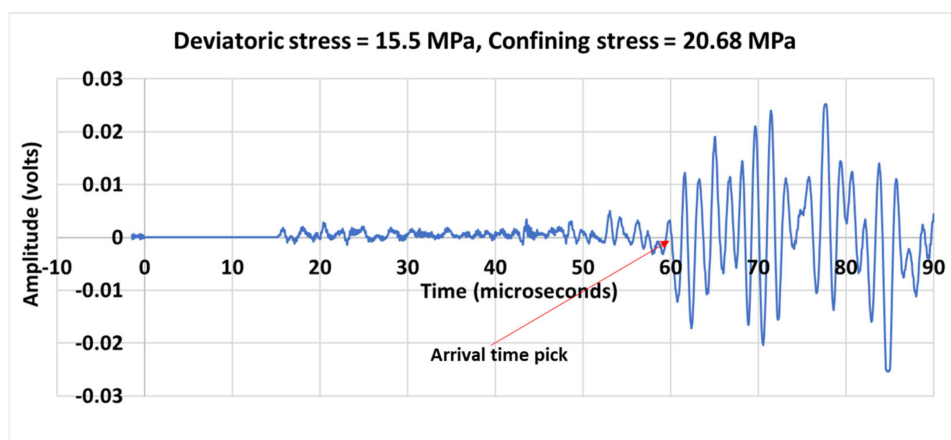
After the vacuum-dried measurement, the sample was again re-equilibrated under vacuum at 80 °C and brine saturated. Figure 2b displays the experimental setup. The pressure vessel was evacuated using a cold trap for 30 min. The sample was then vacuum saturated using de-gassed brine. This ensured that there was no trapped air in the sample. The sample was then pressurized to 6.9 MPa using a compressible chamber, which ensured none of the pressurized confining gas dissolved into the pore space. The sample was then allowed to equilibrate for several days, ensuring full saturation of the pore space. The sample weights before and after the saturation were consistent with a fully fluid-saturated pore space.

The tri-axial test was then repeated on the fully saturated sample while measuring the P- and S-wave velocities. The sample weight before and after the test indicated no significant loss of fluids.

To calibrate the acoustic transducer, we measured the P-wave and S-wave velocities of a known metal. Figure 4 shows the P-wave arrival times measured across 1'', 1.5'', 2'', and 2.5'' aluminum billets. The inverse of the slope is the velocity of aluminum in inch/microsecond, while the intercept is the travel time across the acoustic transducer end caps.



(a)



(b)

Figure 3. (a) Recorded P-wave at confining stress of 20.68 MPa and deviatoric stress of 15.5 MPa of the dry sample. Given the high stresses at which the measurements were made, there was no difficulty in picking the arrival times from the recorded waveforms. P-wave first arrival time pick is also shown in the figure. (b) Recorded S-wave at confining stress of 20.68 MPa and deviatoric stress of 15.5 MPa of the dry sample.

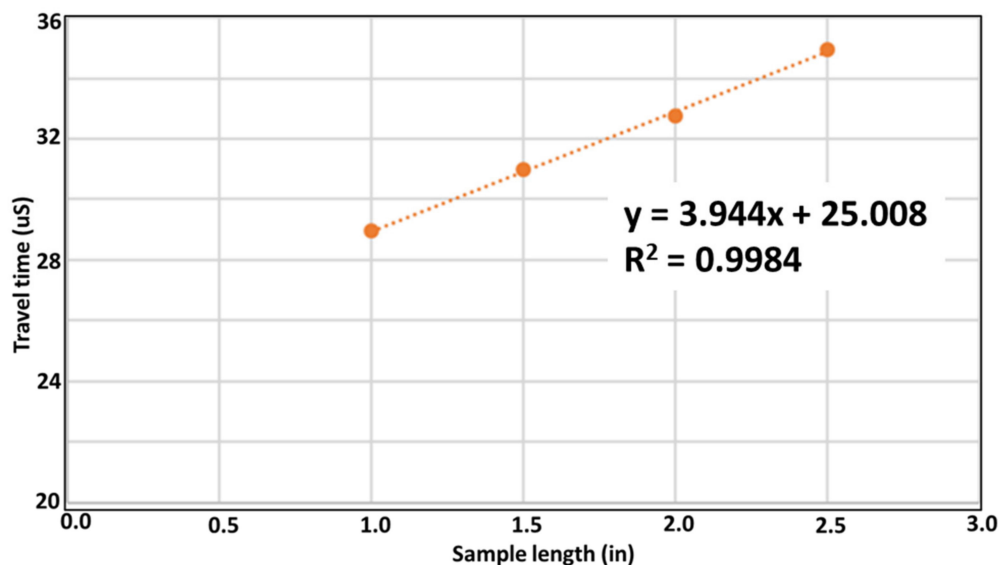


Figure 4. Plot of P-wave arrival times (in microsecond units) measured on 1'', 1.5'', 2'', and 2.5'' Aluminum billets. The inverse of the slope—0.2535 in/us (6.439 km/s)—is the P-wave velocity of aluminum, which is within 0.5% of published P-wave velocity for aluminum (6.42 km/s) [23].

3. Results

3.1. Biot–Gassmann Model Evaluation

Given the measured acoustic P-wave and S-wave velocities and bulk density of the dry rock, we determined the dry-frame bulk and shear modulus. Using Equations (2) and (3) above we computed the Gassmann zero-frequency and Biot high-frequency P-wave velocities. The brine bulk modulus used was 2.43 GPa. Winkler (1985) [13] used a tortuosity value of 2 for Berea sandstone, as did Wang and Nur (1990) [1]. Berea sandstone is more porous and permeable than our core sample. Increasing the value of the tortuosity parameter has the effect of slightly lowering the Biot velocity, which brings it closer to the zero-frequency value, i.e., lowering the dispersion effect. We calculated the Biot high-frequency velocities for a range of values of tortuosity and found the result to be insensitive to this parameter. Table 2 shows the difference between using a value of 2 and 3 for the tortuosity parameters.

Table 2. (a) Percent apparent dispersion. (b) Percent Biot dispersion with tortuosity parameter, α , taken to be 2 or 3.

(a)							
D_A (%)	−1.676	0.220	0.980	1.030	2.448	2.224	
Dev_Stress (MPa)	1.72	15.51	29.32	43.15	56.95	70.95	
(b)							
D_B	1.701	1.751	1.835	1.930	1.950	1.979	$\alpha = 2$
D_B	1.150	1.184	1.240	1.303	1.317	1.336	$\alpha = 3$
Dev_Stress (MPa)	1.72	15.51	29.32	43.15	56.95	70.95	

Figure 5 is a cross plot showing the measured P-wave velocity for the brine-saturated (blue) and dried sample (yellow), as well as the Gassmann (orange) and Biot (gray) predictions. Excepting the sample measurement close to zero deviatoric stress, the measured P-wave velocity for the brine-saturated sample is no higher than 2.5% of the Gassmann P-wave velocity prediction. As shown in Table 2, the apparent percent dispersion (D_A) ranges from −1.67% to 2.4%. These calculated values are all in the order of the measurement error. The Biot dispersion (D_B) is shown in Table 2. It ranges from 1.15% to 1.34% when the tortuosity parameter is 3 and 1.7% to 1.98% when the tortuosity parameter is 2.

The Biot characteristic frequency was determined using Equation (4). The viscosity of the brine, our saturating fluid, was 0.001 Pa·s (1 cp), the permeability was 0.2 microDarcy (or 2×10^{-19} m²), and the brine density was taken to be 1 g/cc. Using these values, the Biot characteristic frequency was calculated to be 4.45×10^{10} Hz, far above the laboratory and logging tool frequencies. This is four orders of magnitude above the laboratory frequency and six orders of magnitude above the logging frequency. This is consistent with the experimental observations shown in Figure 5. We observe that the zero-frequency Gassmann prediction is within 0.2–2.4% of the measured P-wave velocity under ultrasonic frequency; this is close to the experimental error in the measured velocities, which is 1%.

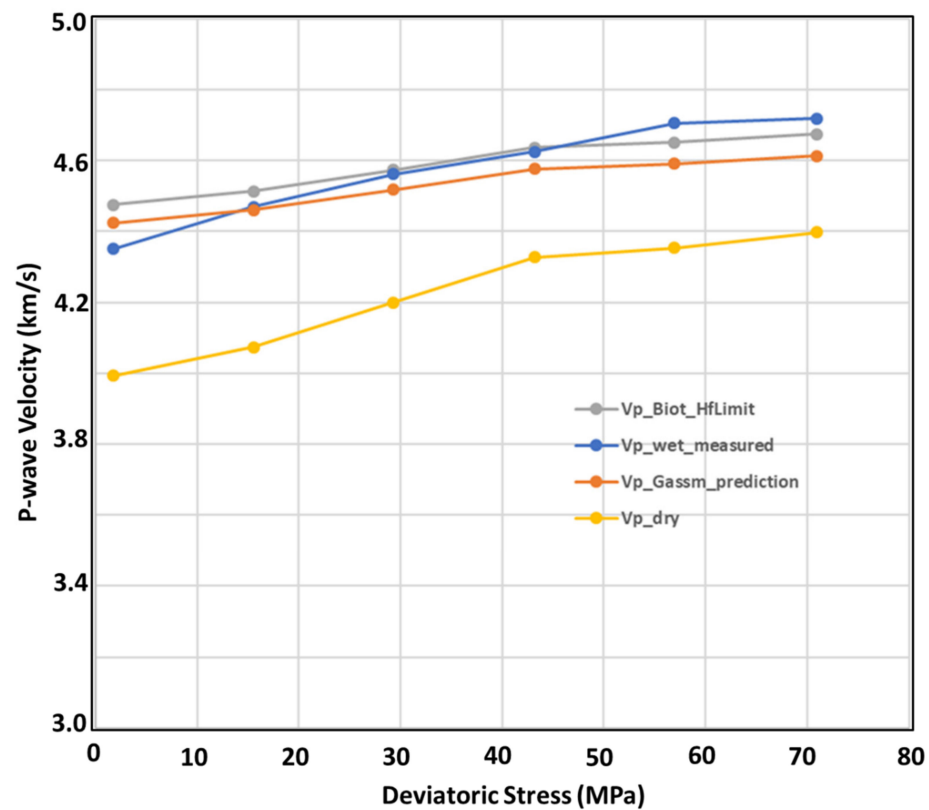


Figure 5. Plot of measured P-wave velocity on brine-saturated sample (blue), Biot P-wave velocity prediction (gray), Gassmann P-wave velocity prediction (orange), and measured P-wave velocity on dry sample (yellow) versus deviatoric stress. Confining pressure was held constant at 20.68 MPa.

3.2. S squirt-Flow Model Evaluation

We applied the detailed squirt-flow computation procedure outlined in Appendix E of Dvorkin et al. (1994) [2] to the acoustic measurements made under a deviatoric stress of 15.5 MPa. The only free parameter, Z , was tuned to match one of four measurements. As recommended by Dvorkin et al. (1994) [2], we used P-wave velocity because it has a larger frequency dispersion than the S-wave velocity. The value of the Z parameter obtained was 5×10^{-6} . This is equivalent to a characteristic squirt-flow length of 30.1 nm, determined from Equation (7). The pore throat radii computed from the Mercury injection capillary pressure data from the core acquired in a close offset well across the same formation range from 2 nm to 150 nm.

$$Z \approx \sqrt{\frac{R^2 \mu \alpha}{k K_s}} \quad (7)$$

with

$$\alpha = 1 - \frac{K_{msd}}{K_s}$$

where R is the characteristic squirt-flow length, K_s is the grain bulk modulus, k is permeability and μ is the viscosity, K_{msd} is the bulk modulus of the dry “modified” rock frame, where modified means that the compliant pores are closed.

Once the Z parameter was determined at the measurement frequency, we computed the P-wave and S-wave velocities and attenuations as a function of frequency, varying frequencies from 10^0 to 10^{15} Hz. Figure 6 is a plot of attenuation versus log frequency. There is no attenuation until $\sim 10^9$ Hz—at which the transition to the high-frequency regime begins. The characteristic frequency is $\sim 10^{11}$ Hz with a Q value of 37. Both the Biot–Gassmann model and the squirt-flow model predict that under in situ stress, the seismic, sonic, and ultrasonic measurement frequencies are all in the low-frequency regime.

In Figure 7, we plot the squirt-flow P-wave and S-wave velocity prediction versus log frequency; both the black discrete data point (Gassmann low-frequency prediction) and the red data point (measured P-wave velocity) are in the squirt-flow low-frequency regime. The percent dispersion when the high-frequency squirt-flow prediction was compared to the measured P-wave velocity under ultrasonic frequency was 3%. The S-wave velocity percent dispersion is 1.6%.

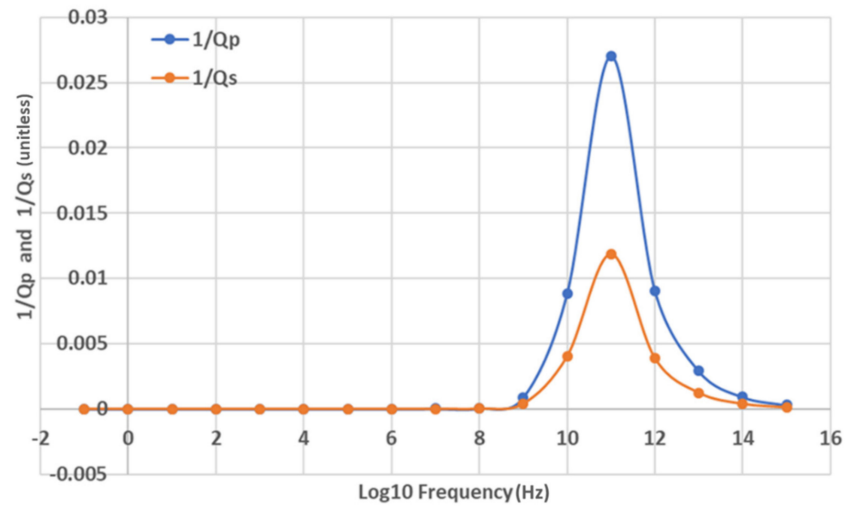


Figure 6. Cross plot of P-wave (blue) and S-wave (orange) attenuation based on Squirt-flow model versus log of frequency (Hz) for the Permian basin sample. Q_p = P-wave quality factor, Q_s = S-wave quality factor.

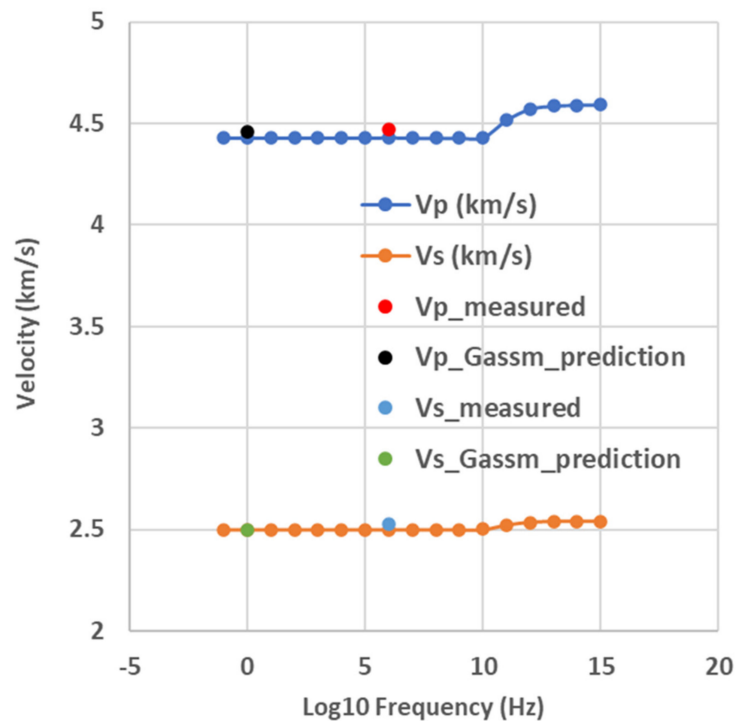


Figure 7. Plot of the squirt-flow P-wave (blue line) and S-wave (orange line) velocity predictions with log frequency. The low-frequency limit P-wave velocity Gassmann prediction is the black data point. The red data point is the measured P-wave velocity at ultrasonic frequency on the fully brine-saturated sample. The blue discrete data point is the measured S-wave velocity on the fully brine-saturated sample, which agrees well with the squirt-flow predicted value. The low-frequency limit S-wave velocity Gassmann prediction is the green data point.

3.3. Cotton Valley Shale Example

The Cotton Valley shale dataset is from Tosaya (1982) [24]. The core was acquired from a depth of 9629 ft (2935 m) in east Texas and described as homogeneous silty shale. The sample mineralogy was 36% clay by volume dominated by illite, 49% quartz, 9.5% feldspars, 3% calcite, 2% siderite, and 0.5% pyrite. The pore fluid used to saturate the sample was deionized water. The pore pressure was kept constant at 1 MPa during the course of this experiment. Figure 8 shows the measured and Biot–Gassmann predictions for the P-wave velocity. The apparent dispersion ranged from -2.73% to -2.03% , which violates the low-frequency Gassmann prediction and may indicate frame softening or measurement error. Tosaya reported that the accuracy of their velocity measurement was 2%. This would imply that the observed difference between the measured data and the Gassmann prediction is consistent with their measurement error (see Appendix A). The stress-dependent predicted Biot dispersion for this sample ranges from 1.18% to 1.34%. The Biot characteristic frequency for the Cotton Valley shale sample was 6.55×10^{10} Hz.

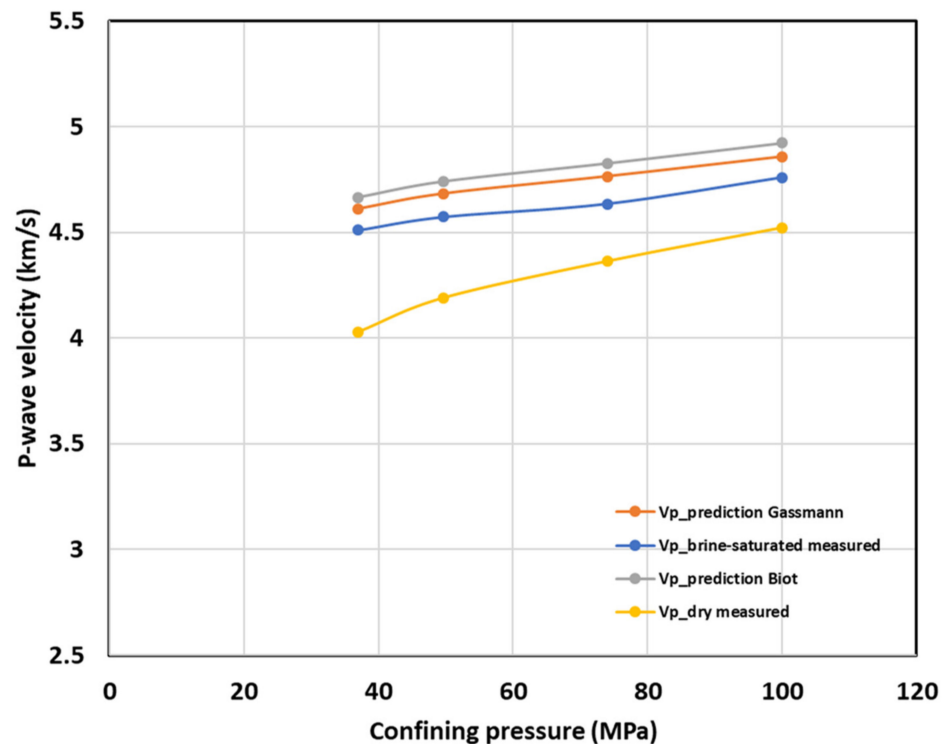


Figure 8. Tosaya (1982) P-wave velocity measurement of Cotton Valley shale. Similar to Figure 5, we have plotted the measured P-wave velocities. (The water-saturated P-wave velocity is in blue, the dry P-wave velocity is in yellow, the Biot P-wave velocity prediction is in gray, the Gassmann P-wave velocity prediction is in orange.) The predicted dispersion is within experimental error.

Applying the squirt-flow model, we used the acoustic measurement at 100 MPa to determine the dry bulk modulus under high confining pressure. This provided a dry modified solid bulk modulus of 22.4 GPa. The measured dry rock P-wave and S-wave velocities at 100 MPa were 4.521 km/s and 3.018 km/s, respectively. We applied the squirt-flow model at the lowest measured stress of 37 MPa, where we expected the squirt-flow-related effect to be the largest. The Z parameter that resulted in a match to P-wave velocity is 2×10^{-6} . This is equivalent to a characteristic squirt-flow length of 7.3 nm (for comparison, water molecule diameter is 0.275 nm; methane molecule is about 0.3988 nm; *n*-butane is 0.415 nm). Figure 9 is a plot of attenuation versus log frequency for the Cotton Valley shale. The plot of P-wave and S-wave velocity prediction versus log frequency is shown in Figure 10.

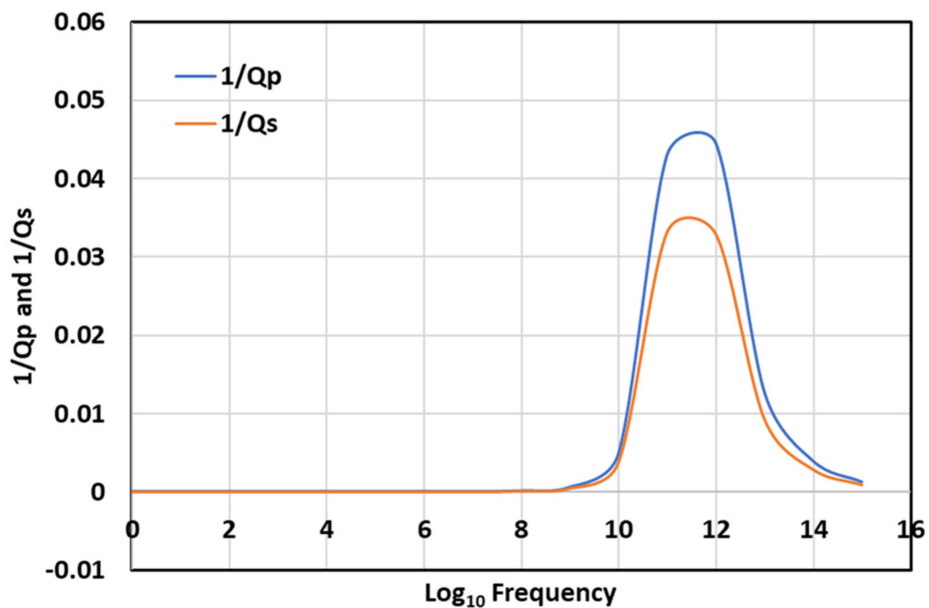


Figure 9. Cross plot of P-wave (blue) and S-wave (orange) attenuation based on Squirt-flow model versus log of frequency (Hz) for the Cotton Valley shale. Q_p = P-wave quality factor, Q_s = S-wave quality factor.

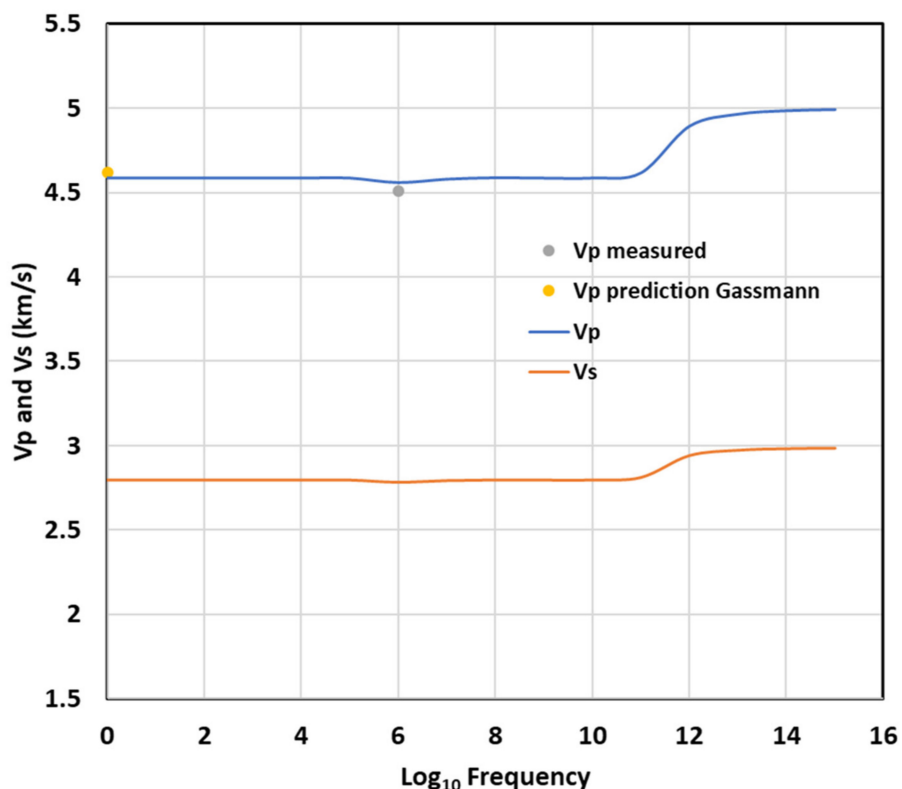


Figure 10. Cotton Valley shale. Cross plot of Squirt-flow P-wave (blue line) and S-wave (orange line) velocity predictions with log of frequency. Yellow data point is the Gassmann P-wave velocity prediction, while the gray data point is the measured P-wave velocity at ultrasonic frequency.

Similar to the Permian-basin example, there is no attenuation until $\sim 10^9$ Hz—, at which the transition to the high-frequency regime occurs. The characteristic frequency is 10^{11} , with a Q value of 21.14. The seismic, sonic, and ultrasonic frequencies are well below the characteristic frequency, i.e., no dispersion is predicted in that frequency range.

3.4. Comparison of Sonic Log to Ultrasonic Frequency measurements

We next compared the sonic log measurements to the laboratory measurements made under ultrasonic frequencies. We have conducted this across several lithofacies and applied the Student *t* distribution to compare if there is a statistically significant difference in the mean values.

While care was taken to preserve the core samples until the laboratory measurements were made, fluid loss during core acquisition cannot be fully eliminated. For all four shale formations described in this section, the in situ fluids are liquid hydrocarbon and brine—no free gas. However, during the process of exhuming the rock from the subsurface—due to decreasing temperature and pressure—liquid hydrocarbon begins to shrink, and dissolved gas bubbles forth. As such, even though there is usually no significant difference between the in situ brine saturation and that measured in the laboratory for these very low-permeability rocks, that is not the case for oil saturation. Especially in the case where the reservoir fluid is a volatile oil, it is not uncommon to measure significant gas saturation in the laboratory (e.g., for the Wolfcamp shale formation example from the Midland basin, the oil formation volume factor is 1.5, while the brine formation volume factor is 1.01).

It is thus necessary to correct the laboratory ultrasonic measurement using the Gassmann equation to the in situ saturation state for appropriate comparison to the in situ sonic log measurements. Core fluid saturation was not measured on twin sample plugs for every one of the ultrasonic core sample measurements in this section. For each shale formation, however, we have reported (see Table 3) and used the average laboratory gas, oil, and brine saturation over the interval compared to the sonic log. The fluid densities and bulk modulus used in Gassmann for fluid substitution to the in situ saturations are given in Table 3. In addition, we also present the combined result of the scenario where the oil saturation is zero (i.e., all the liquid hydrocarbon is lost by the time the ultrasonic measurements were made on the core samples. This rarely occurs if the samples are properly preserved in the field and the gas saturation is zero (no fluid loss, this is also unlikely). The individual shale formation results are no different, but for want of space, we only present the combined result for these two additional scenarios.

Table 3. (a) Average laboratory-measured fluid saturations. S_g is gas saturation, S_o is oil saturation, and S_w is brine saturation. In situ $S_g = 0$ for all four formations considered in this section. Lab $S_w =$ In situ S_w . (b) Fluid Properties required for fluid substitution to in situ fluid saturations.

(a)			
Formation	Average S_g (Dec)	Average S_o (Dec)	Average S_w (Dec)
BSPG_DB	0.40	0.10	0.50
WFMP_DB	0.48	0.17	0.35
WFMP_MB	0.40	0.15	0.45
LSBY_MB	0.40	0.15	0.45
(b)			
Fluid	Density (g/cc)	Bulk Modulus (GPa)	
Brine	1.050	3.200	
Oil	0.700	1.100	
Gas	0.250	0.200	

3.5. Bonespring Formation Example

The average clay volume across the interval of interest is 16%, with the rest being quartz, feldspars, and minor amounts of carbonate. Figure 11 compares the sonic log measured P-wave and S-wave velocities with the ultrasonic measurement acquired at ~1 MHz. The core was depth-shifted to match the log depths. This was conducted by matching the core gamma ray depth—the black curve in the Correlation column—to the well-log gamma ray depth. The laboratory ultrasonic acoustic measurements were made on a 5.08 cm long and 2.54 cm diameter sample; the sonic log measurements have resolutions

that are in the 0.6096 m or higher range; therefore, there is more variation in the core data than the log data was expected.

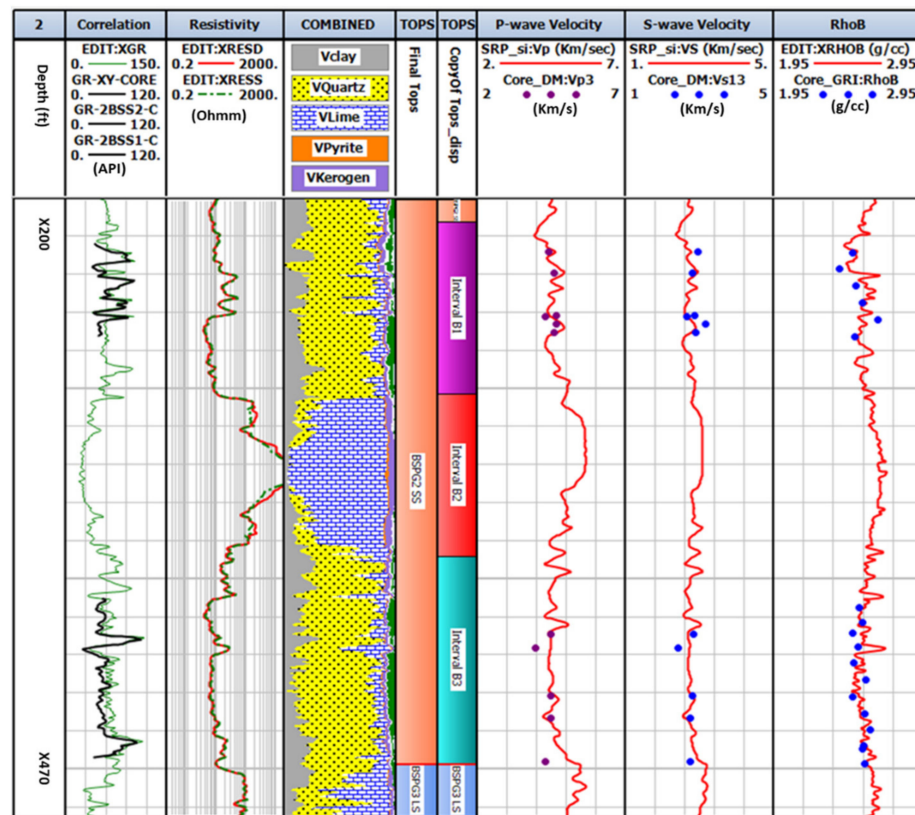


Figure 11. Log plot of the Bonespring formation. The Correlation track contains Gamma-ray (green curve) and core gamma ray (black curve). The Resistivity track contains resistivity log. The COMBINED track contains formation lithology fractional volumes determined by volumetric log analyses. The P-wave velocity track contains sonic P-wave velocity (red curve) and ultrasonic P-wave velocity (purple discrete data points). The S-wave velocity track contains sonic S-wave velocity (red curve) and ultrasonic S-wave velocity (blue discrete data points). The RhoB track contains log measured bulk density (red curve) and core measured bulk density (blue discrete data). Depths in the depth track are only to indicate depth scale; actual depths are not available for publication.

The estimated minimum horizontal in situ confining stress ranges from 13.1 to 15.2 MPa, the estimated maximum horizontal in situ confining stress ranges from 19.3 to 21 MPa. The laboratory data were therefore acquired at an estimated average confining stress of 17.24 MPa and deviatoric stress of 21.4 MPa. Excepting a few data points—which are possibly due to the differences in resolution between the sonic and ultrasonic measurements—there is a good match between both the sonic log and the higher frequency ultrasonic measurements.

We statistically tested for a significant difference in the mean values of these data using the Student *t*-test. To do this, we assumed a Gaussian distribution for both the laboratory and well-log populations. Figure 12 is the histogram of the P-wave velocity for the second Bonespring formation, excluding the limestone interval; the dashed green line is the Gaussian fit to the data. The average of the eleven laboratory-measured ultrasonic P-wave velocities is 4.45 km/s, with a standard deviation of 0.21 km/s. After the fluid substitution to the in situ saturations using Table 3, the average ultrasonic P-wave velocities for the 11 measurements is 4.58 km/s with a standard deviation of 0.186 km/s. The laboratory-measured S-wave velocity mean and the standard deviation are, respectively, 2.81 km/s and 0.18 km/s. After the fluid substitution, the average and standard deviation are, respectively, 2.80 km/s and 0.183 km/s. At the corresponding depths to the ultrasonic core measurements, the mean sonic log P-wave velocity for the second Bonespring formation is

4.63 km/s, with a standard deviation of 0.261 km/s. In comparison, the mean and standard deviation of the sonic log S-wave velocity are, respectively, 2.76 km/s and 0.136 km/s. We address the question of whether there is any significant difference in the estimated means of both datasets using the well-known Student *t*-test. The results for both the P-wave and S-wave velocities are shown in Table 4, and a detailed workflow of how these were obtained is shown in Appendix B. At a confidence level of 99%, we cannot reject the null hypothesis that the means of the sonic log and ultrasonic measurements are the same for both P-wave and S-wave velocities and their ratio (see Table 4).

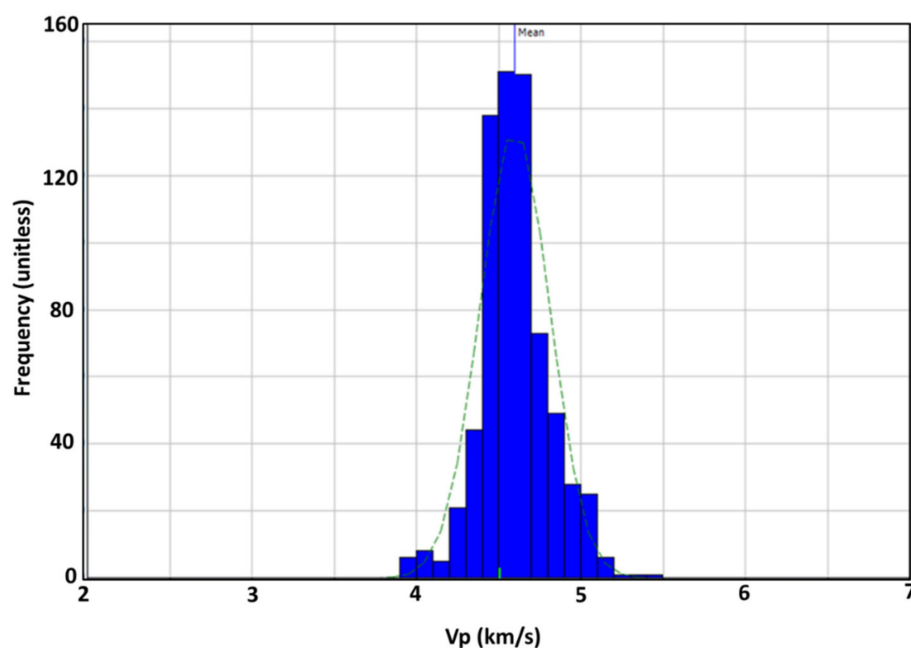


Figure 12. Histogram of the sonic log P-wave velocity in the second Bonespring formation (BSPG2 SS) shown in Figure 9, excluding the limestone interval. Green dashed line is the Gaussian fit to the data.

3.6. Wolfcamp formation—Delaware Basin Example

The Wolfcamp formation example is also from the Delaware basin. The matrix permeability determined through the GRI method ranged from 8 to 120 NanoDarcy. The average clay volume was 15%, and the average total porosity was 8.6%. The laboratory measurements were made under a 17.24 MPa confining stress. The comparison of the sonic log with the ultrasonic measurements is shown in Figure 13. The obvious heterogeneity in the core is shown in Figure 14. These core photos are each about 1.2 ft (0.366 m) in length. Note the significant change in rock facies over an interval that is less than 1 ft (0.3048 m). The vertical core plugs used for the ultrasonic measurements are 2" (5.08 cm) in length, compared to the resolution of the sonic log measurement, which is about 2 ft (0.6096 m). We, therefore, expected a significant variability in the core data as compared to the logs. This is evident in the standard deviation of the core data. The mean laboratory-measured ultrasonic P-wave velocity is 4.27 km/s, with a standard deviation of 0.5 km/s. After the fluid substitution, the mean ultrasonic P-wave velocity is 4.42 km/s, with a standard deviation of 0.417 km/s. The laboratory-measured S-wave velocity mean and the standard deviation (SD) are, respectively, 2.69 km/s and 0.24 km/s, and after the fluid substitution, the mean and standard deviation are, respectively, 2.69 km/s and 0.243 km/s.

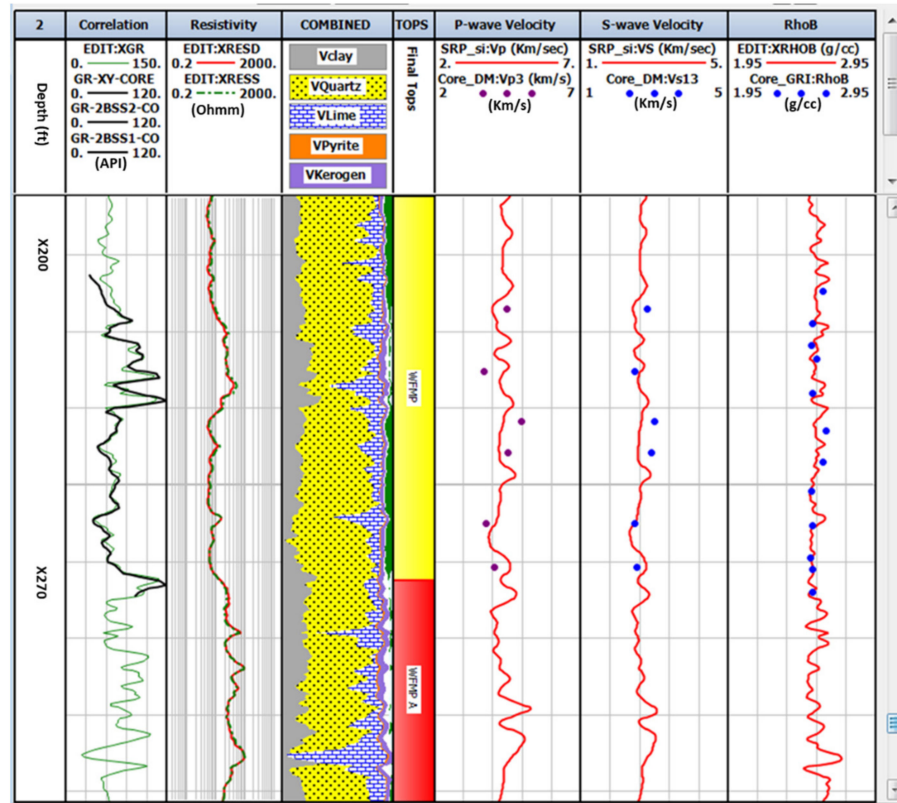


Figure 13. Log plot of the Wolfcamp formation. The correlation track contains log Gamma-ray (green curve) and core gamma ray (black curve). The RESISTIVITY track contains resistivity log. The COMBINED track contains formation lithology fractional volumes determined by volumetric log analyses. The P-wave velocity track contains sonic P-wave velocity (red curve) and ultrasonic P-wave velocity (purple discrete data points). The S-wave velocity track contains sonic S-wave velocity (red curve) and ultrasonic S-wave velocity (blue discrete data points). The RhoB track contains log measured bulk density (red curve) and core measured bulk density (blue discrete data). Depths in the depth track are only to indicate depth scale; actual depths are not available for publication.



Figure 14. Core sample photo from the Wolfcamp cored interval. Sample length for each is 1.2 ft.

Table 4. (a) Student *t*-test result for the co-located sonic log and ultrasonic core P-wave velocity measurements (after fluid substitution to in situ saturations) in the second Bonespring formation. Result indicate there is no significant difference between the mean of the sonic log and ultrasonic core measurements. (b) Student *t*-test result for the co-located sonic log and ultrasonic core S-wave velocity measurements (after fluid substitution to in situ saturations) in the second Bonespring formation. Result indicate there is no significant difference between the mean of the sonic log and ultrasonic core measurements. (c) Student *t*-test result for the co-located sonic log and ultrasonic core V_p/V_s ratio measurements (after fluid substitution to in situ saturations) in the second Bonespring formation. Result indicate there is no significant difference between the mean of the sonic log and ultrasonic core measurements.

(a)		
	V_p_log	V_p_core
Mean	4.63	4.58
Variance	0.068	0.035
Observations	11	11
Pooled Variance	0.051	
Hypothesized Mean Difference	0	
df	20	
t Stat	0.496	
P(T ≤ t) one-tail	0.312	
t Critical one-tail	2.528	
P(T ≤ t) two-tail	0.625	
t Critical two-tail	2.845	
(b)		
	V_s_log	V_s_core
Mean	2.76	2.80
Variance	0.018	0.033
Observations	11	11
Pooled Variance	0.026	
Hypothesized Mean Difference	0	
df	20	
t Stat	−0.560	
P(T ≤ t) one-tail	0.291	
t Critical one-tail	2.528	
P(T ≤ t) two-tail	0.582	
t Critical two-tail	2.845	
(c)		
	V_p/V_s_log	V_p/V_s_core
Mean	1.68	1.64
Variance	0.001	0.003
Observations	11	11
Pooled Variance	0.002	
Hypothesized Mean Difference	0	
df	20	
t Stat	2.095	
P(T ≤ t) one-tail	0.025	
t Critical one-tail	2.528	
P(T ≤ t) two-tail	0.049	
t Critical two-tail	2.845	

|t stat| < t critical; null hypothesis cannot be rejected.

For the corresponding depths, the mean sonic log P-wave velocity for the Wolfcamp formation was 4.27 km/s, with a standard deviation of 0.23 km/s. The mean and standard deviation of the sonic log S-wave velocity are, respectively, 2.58 km/s and 0.14 km/s. The Student *t*-test results are shown in Table 5, and they indicate that we cannot reject the null

hypothesis that the sonic log and the ultrasonic core measurements for the P-wave velocity, S-wave velocity, and their ratio have the same mean value.

Table 5. (a) Student *t*-test for the co-located sonic log and ultrasonic core P-wave velocity measurements (after fluid substitution to in situ saturations) in the Wolfcamp formation, Delaware basin. Result indicate there is no significant difference between the mean of the sonic log and ultrasonic core measurements. (b) Student *t*-test for the co-located sonic log and ultrasonic core S-wave velocity measurements (after fluid substitution to in situ saturations) in the Wolfcamp formation, Delaware basin. Result indicate there is no significant difference between the mean of the sonic log and ultrasonic core measurements. (c) Student *t*-test for the co-located sonic log and ultrasonic core V_p/V_s ratio (after fluid substitution to in situ saturations) in the Wolfcamp formation, Delaware basin. Result indicate there is no significant difference between the mean of the sonic log and ultrasonic core velocity ratios.

(a)		
	V_p _log	V_p _core
Mean	4.27	4.42
Variance	0.052	0.174
Observations	6	6
Pooled Variance	0.113	
Hypothesized Mean Difference	0	
df	10	
t Stat	−0.754	
P(T ≤ t) one-tail	0.234	
t Critical one-tail	2.764	
P(T ≤ t) two-tail	0.468	
t Critical two-tail	3.169	
(b)		
	V_s _log	V_s _core
Mean	2.58	2.69
Variance	0.019	0.059
Observations	6	6
Pooled Variance	0.039	
Hypothesized Mean Difference	0	
df	10	
t Stat	−0.968	
P(T ≤ t) one-tail	0.178	
t Critical one-tail	2.764	
P(T ≤ t) two-tail	0.356	
t Critical two-tail	3.169	
(c)		
	V_p/V_s _log	V_p/V_s _core
Mean	1.66	1.64
Variance	0.000	0.001
Observations	6	6
Pooled Variance	0.001	
Hypothesized Mean Difference	0	
df	10	
t Stat	0.921	
P(T ≤ t) one-tail	0.189	
t Critical one-tail	2.764	
P(T ≤ t) two-tail	0.379	
t Critical two-tail	3.169	

| t stat | < t critical; null hypothesis cannot be rejected.

3.7. Wolfcamp Formation—Midland Basin Example

This Wolfcamp shale formation example is from the Midland basin—a sub-basin of the Permian basin. For the log plot interval shown in Figure 15, the average clay volume is 24%,

and the average total porosity is 7.9%. The matrix permeabilities range from 2 nanoDarcy to 2 microDarcy. The confining stress under which the ultrasonic measurements were made was 13.79 MPa. There is a fairly good match between the in situ sonic log and the laboratory-measured ultrasonic velocities. However, as in the Delaware basin Wolfcamp formation, there is significant lamination within the Wolfcamp shale.

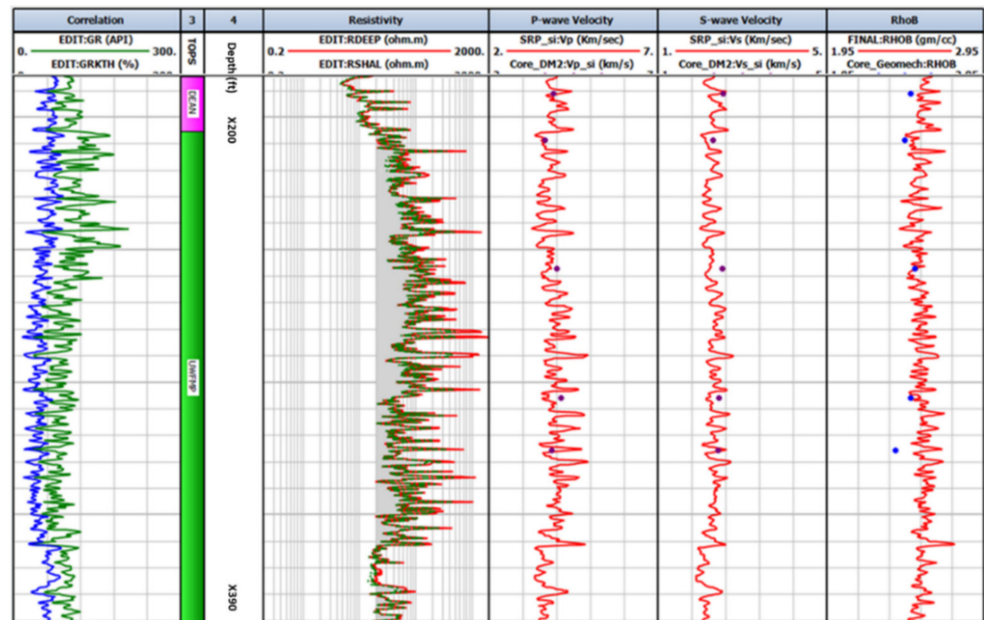


Figure 15. Log plot of the Wolfcamp shale formation—Midland basin. The GAMMA RAY track contains Gamma-ray (green curve) and spectral gamma-ray (blue curve). The RESISTIVITY track contains resistivity log. The P-wave velocity track contains sonic P-wave velocity (red curve) and ultrasonic P-wave velocity (purple discrete data points). The S-wave velocity track contains sonic S-wave velocity (red curve) and ultrasonic S-wave velocity (purple discrete data points). The RhoB track contains log measured bulk density (red curve) and core measured bulk density (blue discrete data). Depths in the depth track are only to indicate depth scale; actual depths are not available for publication.

The mean and standard deviation of the log-measured P-wave velocity are 3.87 km/s and 0.32 km/s, respectively, while the S-wave velocity mean and the standard deviation are 2.29 km/s and 0.18 km/s, respectively. For the P-wave velocity laboratory measurements, the mean and standard deviation are, respectively, 3.90 km/s and 0.18 km/s. The mean laboratory S-wave velocity is 2.45 km/s, with a standard deviation of 0.1km/s. After the fluid substitution, the mean and standard deviation of the laboratory P-wave velocities are, respectively, 4.17 km/s and 0.177 km/s. The S-wave velocity mean and the standard deviation are 2.45 km/s and 0.1 km/s, respectively. The Student *t*-test results are shown in Table 6 for the P-wave, S-wave velocities, and the velocity ratio. They indicate that with a better than 99% confidence, we cannot reject the null hypothesis that the mean of the sonic log measured velocities is equal to the ultrasonic measurements after the fluid substitution despite the observed significant lamination.

Table 6. (a) Student *t*-test for the co-located sonic log and ultrasonic core P-wave velocity measurements (after fluid substitution to in situ saturations) in the Wolfcamp formation, Midland basin. The result indicates there is no significant difference between the mean of the sonic log and ultrasonic core measurements. (b) Student *t*-test for the co-located sonic log and ultrasonic core S-wave velocity measurements (after fluid substitution to in situ saturations) in the Wolfcamp formation, Midland basin. The result indicates there is no significant difference between the mean of the sonic log and ultrasonic core measurements. (c) Student *t*-test for the co-located sonic log and ultrasonic core V_p/V_s ratio (after fluid substitution to in situ saturations) in the Wolfcamp formation, Midland basin. The result indicates there is no significant difference between the mean of the sonic log and ultrasonic core velocity ratios.

(a)		
	V_{p_log}	V_{p_core}
Mean	3.87	4.17
Variance	0.105	0.031
Observations	5	5
Pooled Variance	0.068	
Hypothesized Mean Difference	0	
df	8	
t Stat	−1.835	
P(T ≤ t) one-tail	0.052	
t Critical one-tail	2.896	
P(T ≤ t) two-tail	0.104	
t Critical two-tail	3.355	
(b)		
	V_{s_log}	V_{s_core}
Mean	2.29	2.45
Variance	0.033	0.010
Observations	5	5
Pooled Variance	0.022	
Hypothesized Mean Difference	0	
df	8	
t Stat	−1.652	
P(T ≤ t) one-tail	0.069	
t Critical one-tail	2.896	
P(T ≤ t) two-tail	0.137	
t Critical two-tail	3.355	
(c)		
	V_p/V_{s_log}	V_p/V_{s_core}
Mean	1.69	1.71
Variance	0.001	0.002
Observations	5	5
Pooled Variance	0.002	
Hypothesized Mean Difference	0	
df	8	
t Stat	−0.743	
P(T ≤ t) one-tail	0.239	
t Critical one-tail	2.896	
P(T ≤ t) two-tail	0.479	
t Critical two-tail	3.355	

|t stat| < t critical; null hypothesis cannot be rejected.

3.8. Lower Spraberry Shale Example

The lower Spraberry shale is a liquids-rich Permian-age unconventional reservoir formation in the Midland basin. The average clay volume is 26.6%, and the average total porosity is 6.5% in the lower Spraberry shale interval shown in Figure 16. In Figure 16, the ultrasonic acoustic measurements made on the preserved core samples are compared to the

in situ sonic log measurement. The core data are the discrete data points in the plot, and the ultrasonic measurements shown in the plot are those made under the confining stress that is close to in situ confining stress at the depths sampled. The measurements were made at 15 MPa, estimated under situ confining stress ranging from 12.4 MPa to 15.86 MPa over the sampled interval.

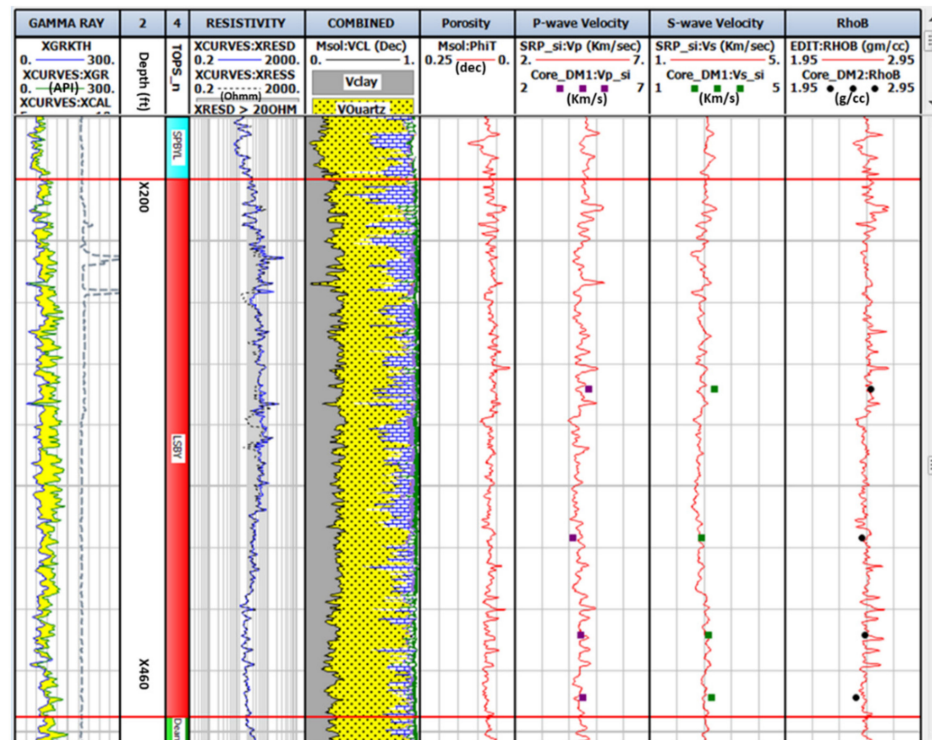


Figure 16. Log plot of the lower Spraberry shale formation. The GAMMA RAY track contains Gamma-ray (green curve) and spectral gamma-ray (blue curve). The RESISTIVITY track contains resistivity log. The COMBINED track contains formation lithology fractional volumes determined by volumetric log analyses. The porosity track contains total porosity. The P-wave velocity track contains sonic P-wave velocity (red curve) and ultrasonic P-wave velocity (purple square discrete data points). The S-wave velocity track contains sonic S-wave velocity (red curve) and ultrasonic S-wave velocity (green discrete data points). The RhoB track contains log measured bulk density (red curve) and core measured bulk density (black discrete data). Depths in the depth track are only to indicate depth scale; actual depths are not available for publication.

At the log depths where we have ultrasonic core measurements, the mean and standard deviation of the sonic log measurements are 4.36 km/s and 0.12 km/s, respectively, for the P-wave velocity, while the S-wave velocity mean and the standard deviation are, respectively, 2.73 km/s and 0.16 km/s. The mean and standard deviation of the laboratory-measured P-wave velocity are 4.44 km/s and 0.25 km/s, respectively; after the fluid substitution, the mean and standard deviation are 4.57 km/s and 0.212 km/s, respectively. The S-wave velocity mean is 2.69 km/s, with a standard deviation of 0.24 km/s; after the fluid substitution, the mean and the standard deviation are 2.73 km/s and 0.074 km/s, respectively. The Student *t*-test results are shown in Table 7 for V_p , V_s , and their ratio. The results indicate that we cannot reject the null hypothesis that the sonic log and ultrasonic core measurements have the same mean value.

Table 7. (a) Student *t*-test for the co-located sonic log and ultrasonic core P-wave velocity measurements (after fluid substitution to in situ saturations) in the lower Spraberry shale formation, Midland basin. The result indicates there is no significant difference between the mean of the sonic log and ultrasonic core measurements. (b) Student *t*-test for the co-located sonic log and ultrasonic core S-wave velocity measurements (after fluid substitution to in situ saturations) in the lower Spraberry shale formation, Midland basin. The result indicates there is no significant difference between the mean of the sonic log and ultrasonic core measurements. (c) Student *t*-test for the co-located sonic log and ultrasonic core V_p/V_s ratio (after fluid substitution to in situ saturations) in the lower Spraberry shale formation, Midland basin. The result indicates there is no significant difference between the mean of the sonic log and ultrasonic core velocity ratios.

(a)		
	V_p _log	V_p _core
Mean	4.36	4.57
Variance	0.014	0.045
Observations	4	4
Pooled Variance	0.030	
Hypothesized Mean Difference	0	
df	6	
t Stat	−1.695	
P(T ≤ t) one-tail	0.071	
t Critical one-tail	3.143	
P(T ≤ t) two-tail	0.141	
t Critical two-tail	3.707	
(b)		
	V_s _log	V_s _core
Mean	2.52	2.73
Variance	0.005	0.026
Observations	4	4
Pooled Variance	0.016	
Hypothesized Mean Difference	0	
df	6	
t Stat	−2.322	
P(T ≤ t) one-tail	0.030	
t Critical one-tail	3.143	
P(T ≤ t) two-tail	0.059	
t Critical two-tail	3.707	
(c)		
	V_p/V_s _log	V_p/V_s _core
Mean	1.73	1.67
Variance	0.003	0.001
Observations	4	4
Pooled Variance	0.002	
Hypothesized Mean Difference	0	
df	6	
t Stat	1.710	
P(T ≤ t) one-tail	0.069	
t Critical one-tail	3.143	
P(T ≤ t) two-tail	0.138	
t Critical two-tail	3.707	

|t stat| < t critical; null hypothesis cannot be rejected.

3.9. Combined Results

For all four of the formations combined (see data in Appendix C), the mean and standard deviation of the sonic log measurements are 4.361 km/s and 0.372 km/s, respectively, for the P-wave velocity, while the S-wave velocity mean and the standard deviation are,

respectively, 2.594 km/s and 0.221 km/s. The mean and the standard deviation of the laboratory-measured P-wave velocity for all four of the formations combined are 4.3 km/s and 0.353 km/s, respectively; after the fluid substitution, the mean and standard deviation are 4.36 km/s and 0.291 km/s, respectively. The S-wave velocity mean is 2.703 km/s, with a standard deviation of 0.219 km/s; after the fluid substitution, the mean and standard deviation are 2.73 km/s and 0.218 km/s, respectively. The Student *t*-test results are shown in Table 8 for the P-wave, S-wave velocities, and the velocity ratio, respectively; as in the case with the individual formations, the results indicate that there is no difference between the mean sonic log and ultrasonic measured P-wave and S-wave velocity measurements.

Table 8. (a) Student *t*-test for the sonic log and ultrasonic core P-wave velocity measurements (after fluid substitution to in situ saturations—labeled as V_{p2} in the following tables) for all four formations combined. The results indicate there is no significant difference between the mean of the sonic log and ultrasonic core measurements. (b) Student *t*-test for the sonic log and ultrasonic core S-wave velocity measurements (after fluid substitution to in situ saturations— V_{s2}) for all four formations combined. The results indicate there is no significant difference between the mean of the sonic log and ultrasonic core measurements. (c) Student *t*-test for the sonic log and ultrasonic core V_p/V_s ratio (after fluid substitution to in situ saturations) for all four shale formations combined. The results indicate that there is no significant difference between the mean of the sonic log and ultrasonic core velocity ratios.

(a)		
	V_{p_log}	V_{p_core}
Mean	4.36	4.46
Variance	0.138	0.085
Observations	26	26
Pooled Variance	0.111	
Hypothesized Mean Difference	0	
df	50	
t Stat	−1.116	
P(T ≤ t) one-tail	0.135	
t Critical one-tail	2.403	
P(T ≤ t) two-tail	0.270	
t Critical two-tail	2.678	
(b)		
	V_{s_log}	V_{s_core}
Mean	2.59	2.70
Variance	0.049	0.048
Observations	26	26
Pooled Variance	0.048	
Hypothesized Mean Difference	0	
df	50	
t Stat	−1.687	
P(T ≤ t) one-tail	0.049	
t Critical one-tail	2.403	
P(T ≤ t) two-tail	0.098	
t Critical two-tail	2.678	
(c)		
	V_p/V_{s_log}	V_p/V_{s_core}
Mean	1.68	1.66
Variance	0.001	0.003
Observations	26	26
Pooled Variance	0.002	
Hypothesized Mean Difference	0	
df	50	
t Stat	1.932	
P(T ≤ t) one-tail	0.030	
t Critical one-tail	2.403	
P(T ≤ t) two-tail	0.059	
t Critical two-tail	2.678	

|t stat| < t critical; null hypothesis cannot be rejected.

In addition, in Table 9, we present the combined result assuming that all of the hydrocarbon liquid is zero during the ultrasonic measurements in the laboratory (i.e., laboratory $S_o = 0$; and laboratory $S_g = 1 - S_w$). Since the core samples were preserved, this scenario

is unlikely. However, it is instructive to conduct the calculations and see, even with this unlikely scenario, if dispersion is observed. Table 9 shows that there is no significant difference between the mean of the in situ sonic log and the ultrasonic measurement after the fluid substitution assuming that all of the liquid hydrocarbon is lost for the P-wave and S-wave velocities, respectively. We similarly observed no significant difference in the mean velocity ratio of the sonic log and the ultrasonic measurements after the fluid substitution.

Table 9. (a) Student *t*-test for the sonic log and ultrasonic core P-wave velocity measurements (after fluid substitution to in situ saturations; with the unlikely assumption that Laboratory $S_o = 0$) for all four formations combined. The results indicate there is no significant difference between the mean of the sonic log and ultrasonic core measurements. (b) Student *t*-test for the sonic log and ultrasonic core S-wave velocity measurements (after fluid substitution to in situ saturations; with the unlikely assumption that Laboratory $S_o = 0$) for all four formations combined. The results indicate there is no significant difference between the mean of the sonic log and ultrasonic core measurements. (c) Student *t*-test for the sonic log and ultrasonic core V_p/V_s ratio measurements (after fluid substitution to in situ saturations; with the unlikely assumption that Laboratory $S_o = 0$) for all four formations combined. The results indicate there is no significant difference between the mean of the sonic log and ultrasonic core velocity ratios.

(a)		
	V_{p_log}	V_{p_core}
Mean	4.36	4.47
Variance	0.138	0.082
Observations	26	26
Pooled Variance	0.110	
Hypothesized Mean Difference	0	
df	50	
t Stat	−1.202	
P(T ≤ t) one-tail	0.118	
t Critical one-tail	2.403	
P(T ≤ t) two-tail	0.235	
t Critical two-tail	2.678	
(b)		
	V_{s_log}	V_{s_core}
Mean	2.59	2.69
Variance	0.049	0.048
Observations	26	26
Pooled Variance	0.048	
Hypothesized Mean Difference	0	
df	50	
t Stat	−1.656	
P(T ≤ t) one-tail	0.052	
t Critical one-tail	2.403	
P(T ≤ t) two-tail	0.104	
t Critical two-tail	2.678	
(c)		
	V_p/V_{s_log}	V_p/V_{s_core}
Mean	1.68	1.66
Variance	0.001	0.003
Observations	26	26
Pooled Variance	0.002	
Hypothesized Mean Difference	0	
df	50	
t Stat	1.582	
P(T ≤ t) one-tail	0.060	
t Critical one-tail	2.403	
P(T ≤ t) two-tail	0.120	
t Critical two-tail	2.678	

|t stat| < t critical; null hypothesis cannot be rejected.

The scenario presented in Table 10 assumes that the in situ saturation state is equivalent to the laboratory saturation state, i.e., we directly compared the in situ sonic log with the laboratory ultrasonic measurements without fluid substitution. This scenario is also unlikely, as there will be some fluid loss due to the decreasing temperature and pressure, especially for volatile oil, when exhuming the rock from the subsurface. However, by

including this scenario, we have essentially sampled all the possible saturation states that could potentially impact the ultrasonic measurements, even though this scenario is not probable. As shown in Table 10, we cannot reject the null hypothesis that the mean of the sonic log and ultrasonic measurements for both the P-wave and S-wave velocities have the same value. However, as shown in Table 10, we did not reach the same conclusion for the velocity ratio, i.e., there is a significant difference between the mean velocity ratio of the sonic log and the ultrasonic measurement when they are compared directly.

Table 10. (a) Student *t*-test for the sonic log and ultrasonic core P-wave velocity measurements (after fluid substitution to in situ saturations; with the very unlikely assumption that Laboratory $S_g = 0$) for all four formations combined. The results indicate there is no significant difference between the mean of the sonic log and ultrasonic core measurements. (b) Student *t*-test for the sonic log and ultrasonic core S-wave velocity measurements (after fluid substitution to in situ saturations; with the very unlikely assumption that Laboratory $S_g = 0$) for all four formations combined. The results indicate there is no significant difference between the mean of the sonic log and ultrasonic core measurements. (c) Student *t*-test for the sonic log and ultrasonic core V_p/V_s ratio measurements (after fluid substitution to in situ saturations; with the very unlikely assumption that Laboratory $S_g = 0$) for all four formations combined. The results indicate that we cannot conclude that there is no significant difference between the mean of the sonic log and ultrasonic core velocity ratios.

(a)		
	V_{p_log}	V_{p_core}
Mean	4.36	4.44
Variance	0.138	0.086
Observations	26	26
Pooled Variance	0.112	
Hypothesized Mean Difference	0	
df	50	
t Stat	-0.854	
P(T ≤ t) one-tail	0.199	
t Critical one-tail	2.403	
P(T ≤ t) two-tail	0.397	
t Critical two-tail	2.678	
(b)		
	V_{s_log}	V_{s_core}
Mean	2.59	2.69
Variance	0.049	0.048
Observations	26	26
Pooled Variance	0.048	
Hypothesized Mean Difference	0	
df	50	
t Stat	-1.640	
P(T ≤ t) one-tail	0.054	
t Critical one-tail	2.403	
P(T ≤ t) two-tail	0.107	
t Critical two-tail	2.678	
(c)		
	V_p/V_{s_log}	V_p/V_{s_core}
Mean	1.68	1.65
Variance	0.001	0.002
Observations	26	26
Pooled Variance	0.002	
Hypothesized Mean Difference	0	
df	50	
t Stat	2.539	
P(T ≤ t) one-tail	0.007	
t Critical one-tail	2.403	
P(T ≤ t) two-tail	0.014	
t Critical two-tail	2.678	

|t stat| < t critical; null hypothesis cannot be rejected.

4. Discussion

Why is it that the squirt-flow model predicts a transition to a higher frequency to be in the 10^9 Hz range, when for more permeable rocks, the squirt-flow effects are observed at much lower frequencies? [18,20,21]. Even in low-permeability rocks, characteristic

frequency has been observed to occur at a much lower frequency. Hoffmann (2005) [4], for example, observed that the transition to higher frequency occurs at about 1000Hz for a high-porosity West Africa shale (low-frequency measurements by Hofmann (2005) [4] were based on a forced oscillator setup). To answer that question, we note that the squirt-flow model predicts that increased dispersion is due to open compliant pores at lower effective stresses. In other words, at relatively higher stresses, when the compliant pores are closed, one is unlikely to observe squirt flow between compliant and stiff pores since the compliant pores will already be closed. Shapiro (2003) [19] concluded that the stress dependencies of the velocities and the elastic moduli are due to the compliant and stiff pores in the rock. The compliant porosity relationship with stress is exponential at relatively higher stresses when all the compliant pores are closed—the relation between stiff porosity and stress is linear. Note the linear change in the porosity with deviatoric stress for our Permian basin sample in Figure 17, indicating that at the stresses, the measurements were made only when the stiff pores were open. That this is the case is also evident in the P-wave velocity versus stress plot in Figure 18.

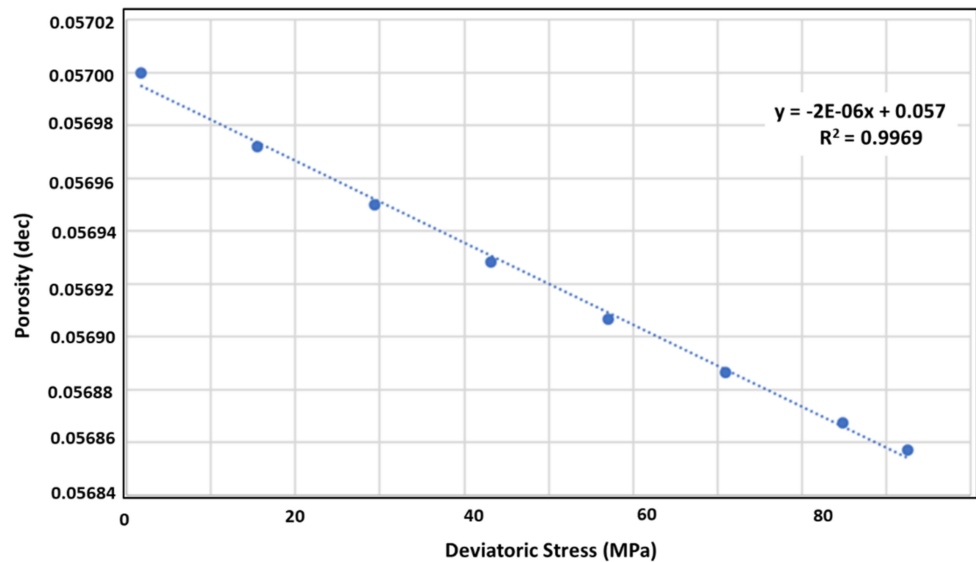


Figure 17. Change in porosity with deviatoric stress for the dry sample measurement at confining stress of 20.68 MPa of our Permian basin rock sample.

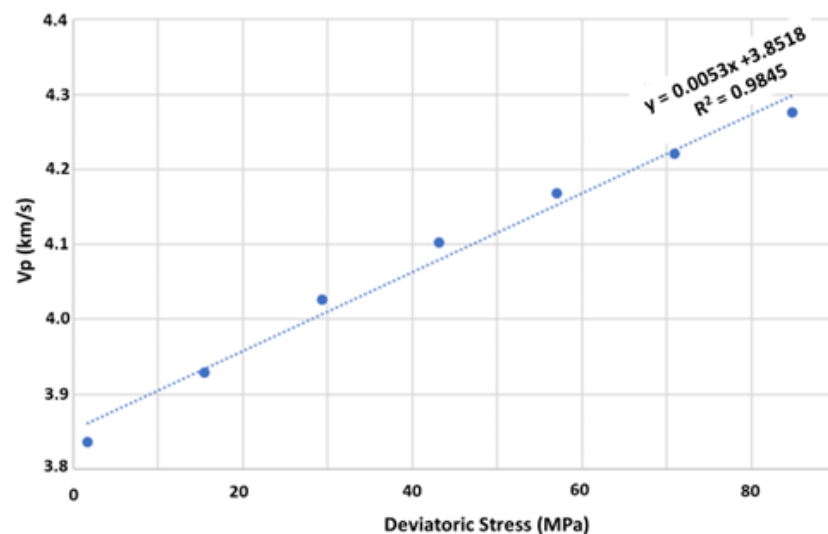


Figure 18. Change in P-wave velocity with deviatoric stress for the dry sample measurement at confining stress of 20.68 MPa of our Permian basin rock sample.

However, de Paula et al. (2012) [21] showed that it is possible to further split the stiff pores into moderately stiff pores (intermediate pores) with an aspect ratio in the 0.001 to 0.2 range and equant pores with an aspect ratio closer to 1. Thus, even when the compliant pores are closed, the squirt flow between the intermediate and equant pores under stresses where the compliant pores are all closed can still occur. We found that we can model all the stiff pores with a single effective aspect ratio [21] of 0.06 using the self-consistent approximation for ellipsoidal inclusions [25]. Using equation 31 from de Paula et al. (2012) [21], the squirt flow due to the intermediate porosity will yield a characteristic frequency of 6.46×10^9 Hz, well above the frequency of ultrasonic experiments in the laboratory. Thus, for our well-consolidated shale samples, the Gurevich (2010) [20] squirt-flow model also predicts that sonic and ultrasonic frequencies are in the same frequency regime.

Our results confirm the experimental observations made by Hofmann (2005) [4] for a low-porosity West Africa shale and by Sarker and Batzle (2010) [8] for the Mancos shale, where they observed no significant dispersion in the measurements made from seismic to ultrasonic frequencies. These results complement ours, including a comparison of the ultrasonic laboratory and the sonic well-log data.

While Liu et al. (1996) [7] also found that the seismic, sonic, and ultrasonic-frequency measurements in shales are also in the same frequency regime, their determination that squirt-flow transition frequency occurs at about 5 Hz is flawed. This is due to the unusually high characteristic squirt-flow length they assumed (10^{-4} m) and used to determine the transition frequency. Loucks et al. (2009) [26], for example, determined from capillary pressure analyses that the dominant pore throat diameter for the low-porosity Barnett shale is in the 5–15 nm range; this is also consistent with the dimensions they measured from SEM (scanning electron microscope) images. Similar nanometer range pore throat diameters have been determined by several other authors for low-porosity shales [27–29] etc.). If, instead, we use the characteristic squirt-flow length we determined for the Cotton Valley shale (7.3 nm) in the example presented in Liu et al. (1994) [7], the transition frequency will be $\sim 10^9$ Hz. Which again will place the seismic, sonic, and ultrasonic frequencies in the same regime and is consistent with what we have determined here.

The positive dispersion effects observed by Szewczyk et al. (2017) [9] are possibly due to their outcrop shale samples having inherent weathering effects. This would require high confining pressures to close the compliant pores and cracks before they would represent a shale under in situ stress conditions [18]. The same reason likely applies to the dispersion effects observed by Hofmann (2005) [4] in their high-porosity West Africa shale sample, i.e., that it is possibly due to the fact that under the stresses their measurements were made, the compliant pores were still open. Best and Sams (1997) [30], for example, noted significant dispersion on near-surface sandstones when the P-wave velocity was measured at low confining pressures and attributed this to the presence of micro-cracks and fractures. Pimienta et al. (2016) [31] made a similar point when they observed that the primary contributor to the magnitude of attenuation is the open micro-cracks. We emphasize that the focus of this study is on well-consolidated shales. In addition, our measurements were made under in situ stress conditions, in part to aid comparison to the in situ sonic log measurements.

Fluid Type

Our rock samples were saturated with low-salinity brine, and the Cotton Valley shale was saturated with deionized water. What if the saturating-fluid filling the rock's pore space were liquid hydrocarbons? Considering live oil, for example, with a viscosity of 0.0005 Pa·s and a density of 500 kg/m³ under in situ conditions. Using Equation (4), the characteristic frequency for this fluid will be 3.78×10^{10} Hz based on the Biot–Gassmann model. This will still be about four orders of magnitude higher than the ultrasonic frequency measurements. If the saturating fluid is dead oil with a viscosity of 0.1 Pa·s and a density of 900 kg/m³ at surface conditions, the Biot model characteristic frequency will be 5.04×10^{12} Hz, which is an even higher frequency when compared to the brine-saturated pore space.

One limitation of our study is that our ultrasonic laboratory data are under-sampled spatially. An area of further research is to explore the possibility of performing sonic and ultrasonic measurements on the same piece of rock. This will address, among other things, the issue of fluid loss when comparing the in situ sonic log measurements with the ultrasonic measurements undertaken in the laboratory.

5. Conclusions

For all of the low-porosity and permeability lithologies discussed in this study, we found no statistically significant intrinsic dispersion due to fluid effects at sonic to ultrasonic frequencies. We expect this to be a general result for unfractured low-permeability well-lithified samples. Under in situ stress conditions, the Gassmann zero-frequency P-wave velocity prediction for the Permian-basin sample was within 0.3% of the measured velocity on the brine-saturated sample under an ultrasonic frequency. We observe similar results for Tosaya's (1982) data in the Cotton Valley shale. Based on the Biot–Gassmann model, we find that the characteristic frequency occurs at about 10^{10} Hz. Applying a squirt-flow model also predicts a transition to the high-frequency regime occurring at about 10^9 Hz for both formations. The comparison of the in situ sonic log measurements for the four different shale/tight rock formations to the ultrasonic measurements made on the core samples under the in situ stress conditions confirms these findings. We cannot reject the hypothesis that there is no significant dispersion due to fluid effects at in situ stress conditions within the frequency range typically used in the petroleum industry. There were differences due to scale effects in the variability of the two datasets. The lack of proven dispersion means that it is justified to compare acoustic measurements at ultrasonic frequencies to measurements made at sonic frequencies without the need for intrinsic dispersion correction. While we have no seismic-frequency measurements to compare to, our modeling using squirt-flow and Biot–Gassmann theory indicates that under normal in situ stress conditions, the compliant pores are closed and, as such, the seismic, sonic, and ultrasonic frequency measurements are all in the same frequency regime for well-consolidated tight rocks. This also implies that dispersion should not be a significant factor affecting the dynamic versus static relationship and that the need for static-dynamic correction is strain magnitude rather than frequency related.

Author Contributions: Conceptualization S.J.O.; Formal Analysis S.J.O., M.M and J.P.C.; Investigation S.J.O., M.M. and J.P.C.; Methodology S.J.O.; Resources M.M.; Writing—original draft S.J.O.; Writing—review and editing M.M and J.P.C. All authors have read and agreed to the published version of the manuscript.

Funding: This research received no external funding.

Data Availability Statement: Data are contained within the article. See also Appendix B.

Acknowledgments: The authors thank Oxy for providing the core samples and log data required to carry out this research.

Conflicts of Interest: The authors declare no conflict of interest.

Appendix A

In this section, we describe how the Student *t*-test results reported for each formation were calculated.

Student t-test: Comparing 2 Independent Samples—Colocated log and Core Datapoints

- Null Hypothesis:

H0. $U_1 - u_2 = 0$, where u_1 is the mean of all sonic log velocity in the formation, and u_2 is the mean of all core measured ultrasonic-velocity measurements in the formation.

Step 1: Compute t -value using the following formula

$$t = \frac{\bar{X}_1 - \bar{X}_2}{s_{\bar{\Delta}}}$$

where

$$s_{\bar{\Delta}} = \sqrt{\frac{s_1^2}{n_1} + \frac{s_2^2}{n_2}}$$

$$d.f. = \frac{\left(\frac{s_1^2}{n_1} + \frac{s_2^2}{n_2}\right)^2}{\frac{s_1^2/n_1}{n_1-1} + \frac{s_2^2/n_2}{n_2-1}}$$

\bar{X}_1 is mean of sample 1

\bar{X}_2 is mean of sample 2

n_1 is number of sample 1 observations

n_2 is number of sample 2 observations

$d.f.$ is degree of freedom

CI confidence interval is 99%

α is 1-CI/100

$$t = \frac{\bar{X}_1 - \bar{X}_2}{s_{\bar{\Delta}}}$$

where:

$$s_{\bar{\Delta}} = \sqrt{\frac{s_1^2}{n_1} + \frac{s_2^2}{n_s}}$$

$$d.f. = \frac{\left(\frac{s_1^2}{n_1} + \frac{s_2^2}{n_2}\right)^2}{\frac{(s_1^2/n_1)^2}{n_1-1} + \frac{(s_2^2/n_2)^2}{n_2-1}}$$

\bar{X}_1 is mean sample 1,

\bar{X}_2 is mean sample 2,

n_1 is number of sample 1 observations,

n_2 is number of sample 2 observations,

s_1 is standard deviation of sample 1,

s_2 is standard deviation of sample 2,

$d.f.$ is degree of freedom

CI confidence interval is 99%

A is 1 - CI/100

Step 2: Compute critical t value (one and two-tail) at df and $\alpha = 0.01$

- If the calculated t -value is greater than the critical t -value, the means are significantly different (compare absolute values)
- Else, if the calculated t -value is less than the critical t -value, we cannot reject the null hypothesis
- Note that while we are only interested in the one-tail test, we have included both the one-tail and two-tail results

Appendix B

Table A1. Sonic log and ultrasonic core measured P-wave and S-wave velocities for the four formations. BSPG_DB is Bonespring formation Delaware basin. WFMP_DB is Wolfcamp formation Delaware basin. WFMP_MB is Wolfcamp formation Midland basin. Furthermore, LSBY_MB is Lower Spraberry formation Midland basin.

Formation	Vp_log	Vs_log	PhiT	Vp_core	Vs_core	RhoB_core
BSPG_DB	km/s	km/s	Dec	km/s	km/s	g/cc
	4.6149	2.7631	0.0883	4.393	2.942	2.48
	4.9093	2.9219	0.1284	4.595	2.807	2.38
	4.4299	2.6105	0.0679	4.678	2.87	2.50
	4.4592	2.6301	0.0667	4.306	2.673	2.55
	4.8568	2.8602	0.039	4.68	3.152	2.65
	4.6876	2.767	0.093	4.61	2.908	2.49
	4.4083	2.6752	0.075	4.495	2.851	2.48
	4.4838	2.7323	0.0678	3.965	2.41	2.52
	4.6315	2.7982	0.0911	4.483	2.793	2.49
	4.3	2.6152	0.0678	4.486	2.748	2.57
	5.1759	3.0407	0.063	4.312	2.759	2.56
	WFMP_DB	3.977	2.4107	0.0728	4.479	2.81
4.3917		2.6189	0.0669	3.708	2.467	2.55
4.3668		2.6447	0.0276	4.986	2.995	2.63
4.2166		2.5494	0.0589	4.528	2.917	2.60
4.0853		2.4548	0.069	3.777	2.454	2.53
4.6032		2.7886	0.065	4.046	2.521	2.54
WFMP_MB	4.039	2.435	0.065	3.891	2.534	2.480
	3.560	2.127	0.084	3.642	2.291	2.440
	3.852	2.221	0.053	3.999	2.527	2.510
	3.575	2.148	0.045	4.132	2.480	2.480
	4.324	2.533	0.046	3.858	2.421	2.390
LSBY_MB	4.249	2.452	0.057	4.725	2.898	2.580
	4.476	2.476	0.065	4.118	2.520	2.520
	4.447	2.614	0.051	4.417	2.714	2.540
	4.269	2.551	0.081	4.501	2.807	2.480

Appendix C

Anisotropic Gassmann Fluid Substitution

While we assumed isotropy in our fluid substitution implementation, most of the rock samples and shale formations we have studied are weakly anisotropic (Thomsen, 1986). The use of the isotropic Gassmann equation is partly motivated by the fact that we often do not measure all the parameters required to fully characterize the stiffness tensor of an anisotropic rock sample. In this section, we seek to determine the errors incurred in assuming isotropy for a weakly anisotropic rock or formation.

For anisotropic porous rock, Gassmann's equation in terms of linear elastic stiffness components is given by (Gassmann, 1951):

$$C_{ijkl}^{sat} = C_{ijkl}^{dry} + \frac{(K_m \delta_{ij} - \frac{C_{ij\alpha\alpha}^{dry}}{3})(K_m \delta_{kj} - \frac{C_{\beta\beta kl}^{dry}}{3})}{\varnothing \left(\frac{K_m}{K_{fl}} \right) (K_m - K_{fl}) + \left(K_m - \frac{C_{ppqq}^{dry}}{9} \right)} \quad (A1)$$

where $\delta_{ij} = 1$, for $i = j$; $\delta_{ij} = 0$, for $i \neq j$.

In rocks having vertical transverse isotropy, Mavko and Bandyopadhyay (2009) came up with an approximate anisotropic fluid substitution equation for vertical P-wave velocity. They also showed, by means of numerical simulation, the validity of the approximate equa-

tion for the Thomsen anisotropic parameter δ as high as 0.3. Mavko and Banyoypadyay's (2009) approximate equation is given below:

$$C_{33}^{sat} \approx C_{33}^{dry} + \frac{\left(\frac{K_{fl}}{K_m}\right) \left[K_m - K_{iso}^{dry} - \left(\frac{2}{3}\right) C_{33}^{dry} \delta\right]^2}{\varnothing \left(K_m - K_{fl}\right) + \left(\frac{K_{fl}}{K_m}\right) \left(K_m - K_{iso}^{dry}\right)} \quad (A2)$$

where K_{iso}^{dry} , K_{fl} , K_m are the elastic bulk moduli of the dry rock, the saturating pore fluid, and the solid mineral, respectively. C_{33}^{sat} and C_{33}^{dry} are the vertical P-wave modulus of the saturated and dry rock, respectively.

For the Cotton Valley shale, Tosaya (1982) obtained the stiffness tensor required to fully characterize this rock. We applied the above equation to the sample measurement under confining stress of 49.63 MPa, for which we have both dry and saturated vertical velocities. The stiffnesses for the saturated measurements are shown in Table A2. We then compared the result to what was obtained, assuming isotropy as shown in Figure 10 in the squirt flow model evaluation sub-section.

Table A2. Cotton Valley shale elastic moduli from Tosaya (1982). Stiffnesses are in GPa.

Pc (MPa)	C11	C33	C66	C13	C44	C12
49.63	66.480	54.280	26.388	24.601	19.089	13.900

The Thomsen anisotropy parameter δ , required in Equation (A2), is given by (Thomsen, 1986):

$$\delta = \frac{(C_{13} + C_{44})^2 - (C_{33} - C_{44})^2}{2C_{33}(C_{33} - C_{44})} \quad (A3)$$

The vertical P-wave velocity determined by applying Equation (A2) is 4.51 Km/s. This yields a 1.4% error when compared to the measured vertical P-wave velocity. This is a significant improvement when compared to the 2.5% error obtained by applying the isotropic Gassmann fluid substitution equation.

References

- Wang, Z.; Nur, A. Dispersion Analysis of acoustic velocities in rocks. *J. Acoust. Soc. Am.* **1990**, *87*, 2384–2395. [[CrossRef](#)]
- Dvorkin, J.; Mavko, G.; Nur, A. Squirt flow in fully saturated rocks. *GEOPHYSICS* **1995**, *60*, 97–107. [[CrossRef](#)]
- Spencer, J.W. Stress relaxations at low Frequencies in fluid-Saturated rocks: Attenuation and modulus dispersion. *J. Geophys. Res.* **1981**, *86*, 1803–1812. [[CrossRef](#)]
- Hofmann, R. Frequency Dependent Elastic and Anelastic Properties of Clastic Rocks. PhD Thesis, Colorado School of Mines, Golden, CO, USA, 2005.
- Sams, M.S.; Neep, J.P.; Worthington, M.H.; King, M.S. The measurement of velocity dispersion and frequency-dependent intrinsic attenuation in sedimentary rocks. *GEOPHYSICS* **1997**, *62*, 1456–1464. [[CrossRef](#)]
- Biot, M.A. Theory of propagation of elastic waves in a fluid saturated porous solid. II higher frequency range. *J. Acoust. Soc. Am.* **1956**, *28*, 179–191. [[CrossRef](#)]
- Liu, X.; Vemik, L.; Nur, A. Effects of saturating fluids on seismic velocities in shale. In *SEG Technical Program Expanded Abstracts 1994*; Society of Exploration Geophysicists: Denver, CO, USA, 1994; pp. 1121–1124. [[CrossRef](#)]
- Sarker, R.; Batzle, M. Anisotropic elastic moduli of the Mancos B Shale—An experimental study. In *SEG Technical Program Expanded Abstracts 2010*; Society of Exploration Geophysicists: Denver, CO, USA, 1994; pp. 1121–1124.
- Szewczyk, D.; Holt, R.M.; Bauer, A. The impact of saturation on seismic dispersion in shales—Laboratory measurements. *GEOPHYSICS* **2017**, *83*, MR15–MR34. [[CrossRef](#)]
- Omovie, S.J.; Castagna, J.P. P-to-S-wave velocity ratio in organic shales. *Geophys.* **2019**, *84*, MR205–MR222. [[CrossRef](#)]
- Wang, Y.; Han, D.-H.; Ren, J.; Zhang, Y.; Zhao, L. Microstructure effects on static and dynamic moduli for two sandstones. In *Proceedings of the Rock Physics and Digital Rock Applications Workshop, Beijing, China, 20–22 May 2018*; Society of Exploration Geophysicists: Denver, CO, USA, 2018; pp. 21–24. [[CrossRef](#)]
- Omovie, S.J.; Castagna, J.P. Relationships between Dynamic Elastic Moduli in Shale Reservoirs. *Energies* **2020**, *13*, 6001. [[CrossRef](#)]
- Winkler, K. Dispersion analysis of velocity and attenuation in Berea sandstone. *J. Geophys. Res.* **1985**, *90*, 6793–6800. [[CrossRef](#)]

14. Peselnick, L.; Outerbridge, W.F. Internal friction in shear and shear modulus of Solenhofen limestone over a frequency range of 107 cycles per second. *J. Geophys. Res.* **1961**, *66*, 581–588. [[CrossRef](#)]
15. Wang, Z.; Wang, H.; Cates, M.E. Effective elastic properties of solid clays. *GEOPHYSICS* **2001**, *66*, 428–440. [[CrossRef](#)]
16. Jaeger, J.C.; Cook, N.G.; Zimmerman, R. *Fundamentals of rock mechanics*; Blackwell Publishing: Malden, MA, USA, 2007.
17. Geertsma, J.; Smit, D.C. Some aspects of elastic wave propagation in fluid-saturated porous solids. *Geophysics* **1961**, *26*, 169–181. [[CrossRef](#)]
18. Mavko, G.; Jizba, D. Estimating grain scale fluid effects on velocity dispersion in rocks. *Geophysics* **1991**, *56*, 1940–1949. [[CrossRef](#)]
19. Shapiro, S.A. Elastic piezosensitivity of porous and fractured rocks. *Geophysics* **2003**, *68*, 482–486. [[CrossRef](#)]
20. Gurevich, B.; Makarynska, D.; de Paula, O.B.; Pervukhina, M. A simple model for squirt-flow dispersion and attenuation in fluid-saturated granular rocks. *Geophysics* **2010**, *75*, 109–120. [[CrossRef](#)]
21. De Paula, O.S.; Pervukhina, M.; Makarynska, D.; Gurevich, B. Modeling squirt dispersion and attenuation in fluid-saturated rocks using pressure dependency of dry ultrasonic velocities. *Geophysics* **2012**, *77*, WA157–WA168. [[CrossRef](#)]
22. Guidry, F.; Luffel, D.; Curtis, J. *Development of Laboratory and Petrophysical Techniques for Evaluating Shale Reservoirs*; GRI (Gas Research Institute) Final Report GRI-95/0496; Gas Research Institute Chicago: Chicago, IL, USA, 1996.
23. Lide, D.R. (Ed.) *CRC Handbook of Chemistry and Physics, Internet Version*; CRC Press: Boca Raton, FL, USA, 2005.
24. Tosaya, C.A. Acoustical properties of clay bearing rocks. Phd Thesis, Stanford University, Stanford, CA, USA, 1982.
25. Berryman, J.G. Long-wavelength propagation in composite elastic media II. Ellipsoidal inclusions. *J. Acoust. Soc. Am.* **1980**, *68*, 1820–1831. [[CrossRef](#)]
26. Loucks, R.G.; Reed, R.M.; Ruppel, S.C.; Jarvie, D.M. Morphology, Genesis, and Distribution of Nanometer-Scale Pores in Siliceous Mudstones of the Mississippian Barnett Shale. *J. Sediment. Res.* **2009**, *79*, 848–861. [[CrossRef](#)]
27. Saidian, M.; Godinez, L.J.; Rivera, S.; Prasad, M. Porosity and Pore Size Distribution in Mudrocks: A Comparative Study for Haynesville, Niobrara, Monterey, and Eastern European Silurian Formations. In Proceedings of the Rock Physics and Digital Rock Applications Workshop, Beijing, China, 20–22 May 2018.
28. Xu, J.; Sonnenberg, S. The Nature of Porosity in Organic-rich Lower Bakken Member and Pronghorn Member, Bakken Formation, Williston Basin. In Proceedings of the 5th Unconventional Resources Technology Conference, Austin, TX, USA, 24–26 July 2017. [[CrossRef](#)]
29. Milliken, K.L.; Rudnicki, M.; Awwiller, D.N.; Zhang, T. Organic matter-hosted pore system, Marcellus Formation (Devonian), Pennsylvania. *AAPG Bull.* **2013**, *97*, 177–200. [[CrossRef](#)]
30. Best, A.I.; Sams, M.S. Compressional wave velocity and attenuation at ultrasonic and sonic frequencies in near-surface sedimentary rocks. *Geophys. Prospect.* **1997**, *45*, 327–344. [[CrossRef](#)]
31. Pimienta, L.; Fortin, J.; Borgomano, J.V.M.; Guéguen, Y. Dispersions and attenuations in a fully saturated sandstone: Experimental evidence for fluid flows at different scales. *Lead. Edge* **2016**, *35*, 495–501. [[CrossRef](#)]